

Durham Research Online

Deposited in DRO:

10 November 2021

Version of attached file:

Published Version

Peer-review status of attached file:

Peer-reviewed

Citation for published item:

Monson, Erik B. and Lehmer, Bret D. and Doore, Keith and Eufrasio, Rafael T. and Bonine, Brett and Alexander, David M. and Harrison, Chris M. and Kubo, Mariko and Mantha, Kameswara B. and Saez, Cristian and Straughn, Amber and Umehata, Hideki (2021) 'On the Nature of AGN and Star Formation Enhancement in the $z = 3.1$ SSA22 Protocluster: The HST WFC3 IR View.', *The Astrophysical Journal*, 919 (1). p. 51.

Further information on publisher's website:

<https://doi.org/10.3847/1538-4357/ac0f84>

Publisher's copyright statement:

© 2021. The American Astronomical Society. All rights reserved

Additional information:

Use policy

The full-text may be used and/or reproduced, and given to third parties in any format or medium, without prior permission or charge, for personal research or study, educational, or not-for-profit purposes provided that:

- a full bibliographic reference is made to the original source
- a [link](#) is made to the metadata record in DRO
- the full-text is not changed in any way

The full-text must not be sold in any format or medium without the formal permission of the copyright holders.

Please consult the [full DRO policy](#) for further details.



On the Nature of AGN and Star Formation Enhancement in the $z = 3.1$ SSA22 Protocluster: The HST WFC3 IR View

Erik B. Monson¹ , Bret D. Lehmer¹ , Keith Doore¹ , Rafael T. Eufrasio¹ , Brett Bonine² , David M. Alexander³ , Chris M. Harrison⁴, Mariko Kubo⁵ , Kameswara B. Mantha⁶, Cristian Saez⁷, Amber Straughn⁸ , and Hideki Umehata^{9,10}

¹Department of Physics, University of Arkansas, 226 Physics Building, 825 West Dickson Street, Fayetteville, AR 72701, USA; ebmonson@uark.edu

²Homer L. Dodge Department of Physics and Astronomy, The University of Oklahoma, 440 W. Brooks Street, Norman, OK 73019, USA

³Centre for Extragalactic Astronomy, Department of Physics, Durham University, South Road, Durham, DH1 3LE, UK

⁴School of Mathematics, Statistics and Physics, Herschel Building, Newcastle University, Newcastle upon Tyne, NE1 7RU, UK

⁵Research Center for Space and Cosmic Evolution, Bunkyo-cho 2-5, Matsuyama, Ehime, 790-8577, Japan

⁶Department of Physics and Astronomy, University of Missouri Kansas City, 202 Flarsheim Hall, 5110 Rockhill Road, Kansas City, MO 64110, USA

⁷Departamento de Astronomía, Universidad de Chile, Casilla 36-D, Santiago, Chile

⁸NASA Goddard Space Flight Center, Code 662, Greenbelt, MD 20771, USA

⁹RIKEN Cluster for Pioneering Research, 2-1 Hirosawa, Wako, Saitama, 351-0198, Japan

¹⁰Institute of Astronomy, Graduate School of Science, The University of Tokyo, 2-21-1 Osawa, Mitaka, Tokyo 181-0015, Japan

Received 2021 February 12; revised 2021 June 10; accepted 2021 June 25; published 2021 September 23

Abstract

We examine possible environmental sources of the enhanced star formation and active galactic nucleus (AGN) activity in the $z = 3.09$ SSA22 protocluster using Hubble WFC3 F160W ($\sim 1.6 \mu\text{m}$) observations of the SSA22 field, including new observations centered on eight X-ray selected protocluster AGN. To investigate the role of mergers in the observed AGN and star formation enhancement, we apply both quantitative (Sérsic-fit and Gini- M_{20}) and visual morphological classifications to F160W images of protocluster Lyman-break galaxies (LBGs) in the fields of the X-ray AGN and $z \sim 3$ field LBGs in SSA22 and GOODS-N. We find no statistically significant differences between the morphologies and merger fractions of protocluster and field LBGs, though we are limited by small number statistics in the protocluster. We also fit the UV-to-near-IR spectral energy distributions of F160W-detected protocluster and field LBGs to characterize their stellar masses and star formation histories. We find that the mean protocluster LBG is a factor of ~ 2 times more massive and more attenuated than the mean $z \sim 3$ field LBG. We take our results to suggest that ongoing mergers are not more common among protocluster LBGs than field LBGs, though protocluster LBGs appear to be more massive. We speculate that the larger mass of the protocluster LBGs contributes to the enhancement of SMBH mass and accretion rate in the protocluster, which in turn drives the observed protocluster AGN enhancement.

Unified Astronomy Thesaurus concepts: High-redshift galaxy clusters (2007); High-redshift galaxies (734); Active galactic nuclei (16); X-ray active galactic nuclei (2035); Galaxy mergers (608)

Supporting material: extended figure, machine-readable table

1. Introduction

Galaxy clusters, the largest virialized, gravitationally bound structures in the universe, are currently thought to form by the dark-matter-driven mergers of protoclusters, smaller groupings of galaxies in the early universe (i.e., $z \gtrsim 2$; lookback times $\gtrsim 10$ Gyr). In current cosmological models, the most luminous modern galaxies are assembled in protoclusters by mergers of smaller galaxies, where gas-rich mergers may trigger active galactic nuclei (AGNs) and episodes of star formation. These protoclusters can move along dark matter filaments toward dense nodes, where they merge and collapse to form the clusters observed at lower redshifts (e.g., Boylan-Kolchin et al. 2009). Protoclusters have been discovered at redshifts ranging from $z \sim 2$ (e.g., Venemans et al. 2002; Miley et al. 2004; Capak et al. 2011; see Overzier 2016 for a review) as far as $z \sim 8$ (in the BoRG58 field; Trenti et al. 2012), in the epoch of galactic reionization, less than 1 Gyr after the Big Bang. Observations of protoclusters provide direct constraints on galaxy evolution, supermassive black hole (SMBH) growth, and the formation of large-scale structures and their galactic constituents.

The protocluster in the SSA22 survey field (R.A.: $22^{\text{h}}17^{\text{m}}34^{\text{s}}.7$, decl.: $+0^{\circ}15'7''$; Cowie et al. 1994) was discovered by Steidel et al. (1998) as a spike in the redshift distribution of Lyman-break

galaxies (LBGs) at $z = 3.09$. Further observations of the same region revealed a \sim six-fold overdensity of LBGs consistent with a galaxy cluster in the early stages of development (Steidel et al. 2000, 2003). Simulations suggest that the SSA22 protocluster and structures of similar scale and overdensity will evolve toward Coma-like (virialized mass $\sim 10^{14} M_{\odot}$) clusters at redshift $z = 0$ (Governato et al. 1998). Recent surveys (e.g., Toshikawa et al. 2016, 2018; Higuchi et al. 2019) of candidate protoclusters suggest that progenitors of Coma-like clusters are not uncommon, with perhaps 76% of 4σ significant overdensities projected to evolve into clusters with masses $\sim 5 \times 10^{14} M_{\odot}$, though conclusive spectroscopic identifications of protoclusters remain difficult and possibly biased toward younger galaxies due to the reliance on Ly α emission (Toshikawa et al. 2016, 2018).

Follow-up narrowband observations over an area 10 times larger than that studied in Steidel et al. (1998) using SUPRIME-Cam have further identified \sim six-fold overdense bands of Ly α emitting galaxies (LAEs), spectroscopically confirmed as a set of three large-scale filamentary structures (Hayashino et al. 2004; Matsuda et al. 2005). The comoving scale of the largest of these filaments, shown in Figure 1, is on the order of 60 Mpc long and 10 Mpc wide, with a redshift range of 3.088–3.108, making it one of the largest mapped structures at $z \sim 3$ (Matsuda et al. 2005). Large Ly α emitting

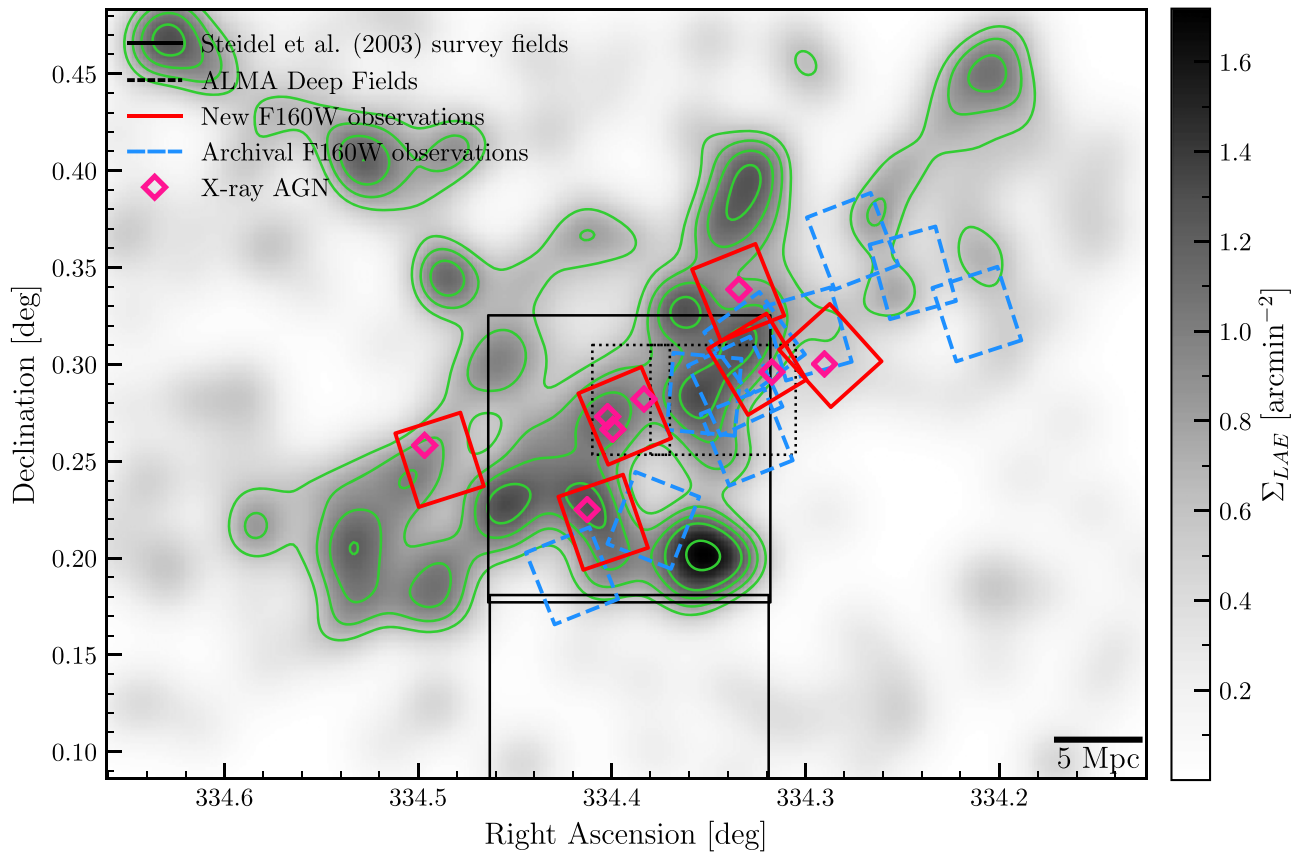


Figure 1. Rectangles show the position and orientation of our observations (thick red lines) and archival observations (dashed blue lines) relative to the protocluster, which is shown as a surface density map of $z = 3.1$ LAEs from Hayashino et al. (2004). To highlight the general shape of the protocluster, we also show contours at levels $\{0.6, 0.8, 1.0, 1.2, 1.6\} \text{ arcmin}^{-2}$. We show the positions of the eight X-ray detected protocluster AGN from Lehmer et al. (2009b) and Alexander et al. (2016) as open magenta diamonds. For reference, we also show the SSA22 fields studied in Steidel et al. (2003) (their SSA22a and SSA22b) in solid black lines, the approximate footprints of the ALMA deep fields studied by Umehata et al. (2015, 2017, 2018, 2019) in dotted black lines, and a 5 comoving Mpc scalebar.

nebulae ($\text{Ly}\alpha$ blobs; LABs) around star-forming galaxies have been shown to be associated with these filaments, suggesting that they are the precursors of massive galaxies developing in the regions of greatest overdensity (Matsuda et al. 2005). The filamentary structure of the protocluster has been further established by MUSE spectral-imaging observations mapping the filaments in emission around the protocluster core (Umehata et al. 2019). The scale and detail at which the filamentary structures in SSA22 have been mapped remains relatively unique among high-redshift protoclusters, though this is also changing: Harikane et al. (2019) mapped candidate protoclusters at $z > 6$ on scales of > 100 comoving Mpc, and Daddi et al. (2021) have recently imaged filamentary structures in $\text{Ly}\alpha$ emission around an overdensity of galaxies at $z = 2.9$.

The SSA22 region has also been well-studied in millimeter/submillimeter bands (Tamura et al. 2009; Umehata et al. 2014, 2015, 2017, 2018, 2019; Alexander et al. 2016). Umehata et al. (2015) identified a concentration of eight dusty star-forming galaxies (DSFGs) associated with the intersection of the major filamentary structures at the center of the protocluster. *Herschel* SPIRE measurements suggest that DSFGs in the SSA22 protocluster account for a star formation rate density on the order of $10^3 M_\odot \text{ yr}^{-1} \text{ Mpc}^{-3}$, a factor of $\sim 10^4$ increase in star formation rate density over the field at redshift $z = 3.09$ (Kato et al. 2016). Additionally, five of the SSA22 DSFGs are associated with X-ray luminous AGN, and two are associated with LABs. Further observations of the

protocluster core with higher-resolution submillimeter instruments have revealed more DSFGs, at least 10 of which are spectroscopically confirmed protocluster members, possibly indicating preferential formation of these galaxies in the densest region of the protocluster (Umehata et al. 2017, 2018). Wide-spectrum (u^* -band to Spitzer IRAC $8 \mu\text{m}$) photometry and spectral energy distribution (SED) fitting by Kubo et al. (2013) has additionally suggested the presence of very massive galaxies in the densest regions of the protocluster. Overall, these observations support a picture of the SSA22 protocluster environment as one where massive, intensely star-forming galaxies are actively forming.

Chandra X-ray observations of the region have revealed a higher rate of AGN activity compared to field galaxies at $z \sim 3$ (Lehmer et al. 2009b), with $9.5^{+12.7}_{-6.1}\%$ and $5.1^{+6.8}_{-3.1}\%$ of protocluster LBGs and LAEs, respectively, hosting AGN with $L_{8-32 \text{ keV}} \gtrsim 3 \times 10^{43} \text{ erg s}^{-1}$. These fractions are elevated by a factor of ≈ 6 compared to non-protocluster galaxies (hereafter, “field” galaxies) at $z \sim 3$, indicating a possible enhancement of SMBH growth in the protocluster. Similar enhancements have been observed in other $z = 2-4$ protoclusters (e.g., HS1700, Digby-North et al. 2010; 2QZCluster, Lehmer et al. 2013; DRC, Vito et al. 2020); there is also evidence that AGN fraction in overdense environments evolves with redshift (Martini et al. 2013), with overdensities at higher redshifts having larger AGN fractions and modern clusters having lower AGN fractions than the field.

The AGN and highly star-forming galaxies in the protocluster are consistently found to be associated with the larger-scale structure of the protocluster, embedded in the intersection of the filaments and giant Ly α nebulae. Of the eight X-ray detected protocluster AGN from Lehmer et al. (2009b), four are associated with LABs, two of which are giant LABs larger than 100 kpc in scale (Alexander et al. 2016). The implication, then, is that the enhanced AGN and star formation activity are driven by environmental factors unique to the protocluster. These enhancements may be driven by accretion episodes caused by an elevated merger rate among protocluster members, or by secular gas accretion from shared gas reservoirs (Narayanan et al. 2015) and filamentary structures in the intergalactic medium (Umehata et al. 2019). However, the AGN enhancement may also be driven by the presence of more massive galaxies (and hence SMBH) in the protocluster, as compared to the field at $z \sim 3$; it has been established that galaxies in $2 \lesssim z \lesssim 4$ protoclusters are on average more massive than their field counterparts at the same redshift (e.g., Steidel et al. 2005; Hatch et al. 2011; Cooke et al. 2014).

Motivated by the elevated AGN fraction observed in the protocluster, Hine et al. (2015) used archival Hubble ACS F814W optical observations of SSA22 (probing rest-frame UV emission) to visually classify LBGs in the protocluster, finding a marginally enhanced merger fraction among protocluster galaxies ($48\% \pm 10\%$) as compared to field galaxies ($30\% \pm 6\%$). However, these results are limited by the small number statistics of the protocluster and suffer from ambiguous interpretation due to the patchiness of rest-frame UV observations, which are highly influenced by star formation activity and attenuation. High-resolution near-infrared (i.e., 1–2 μm) observations, which probe rest-frame optical wavelengths at $z = 3.09$, can better trace the stellar mass content of the protocluster galaxies, less influenced by individual bursts of star formation and more sensitive to merger activity.

In this work, we investigate the possible contributions of mergers to the increased AGN and SF activity in the protocluster by applying three separate morphological analysis techniques to galaxies detected in Hubble WFC3 infrared (F160W, $\lambda_p = 1.537 \mu\text{m}$) observations in SSA22, targeting the environment around the X-ray detected protocluster AGN studied in Alexander et al. (2016). We use parametric model fitting techniques to extract Sérsic model parameters from F160W-detected LBGs, compare the measured morphologies of protocluster LBGs to a sample of field LBGs in GOODS-N, and analyze the residuals after Sérsic model subtraction for indications of merger activity. We additionally use nonparametric morphological measures (the Gini coefficient G , moment of light M_{20} , and concentration C) to compare the morphologies of protocluster and field galaxies and attempt to classify mergers. Finally, we apply a visual analysis similar to that of Hine et al. (2015) to our sample of F160W-detected LBGs, to compare the rest-frame optical merger fraction for the SSA22 protocluster to the field at $z \sim 3$.

We also investigate the possibility that more massive galaxies are the driver of AGN and SF enhancement by fitting the SEDs of a subset of our F160W-detected SSA22 LBG sample. We compare the distribution of stellar mass and the mean star formation history of protocluster LBGs to a sample of $z \sim 3$ field LBGs in GOODS-N.

The paper is organized as follows: Section 2 describes the observations, data reduction, catalog generation, and sample

selection; Section 3 describes our analysis of the morphological properties of protocluster galaxies; Section 4 describes our analysis of the SEDs and physical properties of protocluster galaxies; in Section 5, we discuss our results and attempt to connect the morphologies and physical properties of protocluster galaxies to the protocluster environment; last, in Section 6, we summarize our results and their implications for understanding the galaxy assembly process at $z \sim 3$.

Coordinates in this work are J2000, magnitudes are given in the AB system, and we adopt a Kroupa (2001) IMF. We adopt a cosmology with $H_0 = 70 \text{ km s}^{-1} \text{ Mpc}^{-1}$, $\Omega_M = 0.3$, and $\Omega_\Lambda = 0.7$, yielding a lookback time of 11.42 Gyr, a 2.04 Gyr universe age, and a physical scale of 7.63 proper kpc arcsec $^{-1}$ at $z = 3.09$. We use proper scales when discussing lengths on the scale of galaxies, and comoving scales when discussing lengths on the scale of the protocluster itself. Hereafter, we define SSA22 protocluster galaxies as those galaxies in our F160W images with $3.06 \leq z \leq 3.12$. Over this range of redshift, the rest-frame wavelength probed by our WFC3 IR observations ranges from 3740 to 3790 Å.

2. Data Analysis

2.1. Data Reduction

We use 16 HST WFC3 F160W images of the SSA22 field for our morphological analyses (HST proposals 13844, 11735, 11636, 14747). We summarize the locations and exposure times of these fields in Table 1, and show their footprints superimposed on the protocluster structure in Figure 1. Six of these fields (HST proposal 13844) were new observations obtained to cover the eight protocluster AGN detected in Chandra observations by Lehmer et al. (2009b) that were studied by Alexander et al. (2016). These six observations were taken at two-orbit depth for ease of comparison to the CANDELS-Wide fields (Grogin et al. 2011; Koekemoer et al. 2011).

The STScI AstroDrizzle package¹¹ was used for image recombination and data reduction. We rebin our images to a scale of $0''.065 \text{ pixel}^{-1}$; at this scale, the PSF FWHM of the images is ≈ 2.6 pixels. We adopt an inverse variance weighting scheme when combining the exposures. We use the inverse variance weight maps generated by AstroDrizzle to create a map (a “sigma image”) of the estimated total standard deviation (in electrons) for each pixel in the sky-subtracted science image as

$$\sigma = \sqrt{p_{>0} + \frac{1}{\text{weight}}},$$

where $p_{>0}$ denotes the greater of the science image pixel value (in electrons) and zero.

We adopt a model PSF based on the median of 33 isolated stars in our two-orbit depth WFC3 F160W images, identified using SExtractor (Bertin & Arnouts 1996) by making a box selection in the MAG_AUTO–FLUX_RADIUS plane; we select sources with $0''.13 < \text{FLUX_RADIUS} < 0''.15$ and $21.1 < \text{MAG_AUTO} < 22.8$ as stars.

¹¹ <http://drizzlepac.stsci.edu>

Table 1
Summary of HST WFC3 F160W Survey Fields

| ID | R.A. (deg) | Decl. (deg) | Pos. Angle (deg) | Exp. Time (s) | Proposal No. | PI |
|------------------------------------|---------------|----------------|---------------------|------------------|--------------|-----------|
| New Observations ^a | | | | | | |
| TARGET1 | 334.29 | 0.3046 | −47.95 | 5223.50 | 13844 | Lehmer |
| TARGET2 | 334.32 | 0.3001 | 121.10 | 5223.50 | 13844 | Lehmer |
| TARGET3 | 334.33 | 0.3371 | 111.91 | 5223.50 | 13844 | Lehmer |
| TARGET4 | 334.39 | 0.2734 | −67.27 | 5223.50 | 13844 | Lehmer |
| TARGET5 | 334.40 | 0.2185 | −71.17 | 5223.50 | 13844 | Lehmer |
| TARGET6 | 334.49 | 0.2507 | −72.31 | 5223.50 | 13844 | Lehmer |
| Archival Observations ^b | | | | | | |
| SSA22AC6M4 | 334.42 | 0.1908 | 111.75 | 2611.75 | 11735 | Mannucci |
| SSA22AC30 | 334.33 | 0.2624 | 111.77 | 2611.75 | 11735 | Mannucci |
| SSA22AM16 | 334.38 | 0.2194 | 68.60 | 2611.75 | 11735 | Mannucci |
| SSA22AM38C48 | 334.33 | 0.3109 | 126.09 | 2611.75 | 11735 | Mannucci |
| SSA-22A-IR | 334.34 | 0.2888 | 115.00 | 2611.75 | 11636 | Siana |
| SSA-22A-IR2 | 334.35 | 0.2846 | 85.00 | 2611.75 | 11636 | Siana |
| SSA22.4.IR | 334.21 | 0.3260 | 108.00 | 2611.75 | 14747 | Robertson |
| SSA22.5.IR | 334.24 | 0.3473 | −74.60 | 2611.75 | 14747 | Robertson |
| SSA22.6.IR | 334.28 | 0.3636 | 111.00 | 2611.75 | 14747 | Robertson |
| SSA22.7.IR | 334.30 | 0.3157 | 106.00 | 2611.75 | 14747 | Robertson |

Notes.

^a Shown in red in Figure 1.

^b Shown in blue in Figure 1.

2.2. Catalog Generation

We use GALAPAGOS-2 (Barden et al. 2012; Häussler et al. 2013) to carry out source detection (using SExtractor), background determination, model fitting (using GALFIT, an updated multiband version of GALFIT; see Vika et al. 2013), and catalog compilation. We briefly describe the methods adopted for the catalog generation tasks here, since they are relevant to our methodology (for a more thorough description, see Barden et al. 2012).

SExtractor is designed to deblend sources so that nearby sources are detected and cataloged separately. To prevent over-deblending of bright sources while still detecting faint sources in deep images, GALAPAGOS-2 runs SExtractor twice, once with a low threshold for detection and once with a high threshold. Detections from the high-threshold run are accepted and cataloged automatically; detections from the low-threshold run are rejected if they fall inside the isophotal ellipse of a high-run source, and accepted otherwise. Science image and sigma image cutouts are then constructed for each source.

SExtractor is known to overestimate the sky level (Häussler et al. 2007), so GALAPAGOS-2 determines a local sky value of its own and holds the sky fixed during the later model-fitting step. The procedure is described in detail in Barden et al. (2012). Briefly, GALAPAGOS-2 identifies the brightest secondary sources in each cutout, enlarges their SExtractor Kron isophotes by a predetermined factor (default 2.5 times), masks out every pixel inside the resulting ellipses, and takes the median of the remaining pixels as the local background.

To generate our preliminary source catalog, the detection criteria for the “hot” low-threshold run was 15 pixels $\geq 2.5\sigma$ above the background after convolution with a Gaussian kernel with an FWHM of 2 pixels (i.e., the default 5×5 pixel

Gaussian kernel supplied with SExtractor). For the “cold,” high-threshold run, the detection criteria were strengthened to 30 pixels $\geq 3.5\sigma$ above the background; no convolution filter was applied on the cold run. Sources were deblended using 64 thresholds and a minimum contrast of 0.001. The SExtractor Kron isophotes were enlarged by a factor of 2.5 when combining the hot and cold catalogs.

To estimate the completeness of our preliminary catalog under these SExtractor parameters, we added a total of 3000 simulated stars and 3000 simulated galaxies (generated using GALFIT, with morphological parameters uniformly selected from ranges taken from the van der Wel et al. (2012) fits to $z \sim 3$ GOODS-N galaxies) to our two-orbit images and redetected them with the same procedures. We find that our preliminary catalog is 90 (50) percent complete to an F160W magnitude of 24.8 (25.7) for galaxies and 25.1 (26.2) for point sources detected in two-orbit images. We repeated the process for the single-orbit images, finding 90 (50) percent completeness limit magnitudes of 24.7 (25.4) for galaxies and 24.8 (26.0) for point sources.

To clean spurious or unphysical SExtractor detections from the catalog, we require detections to have signal-to-noise ratio (S/N) ≥ 5 in a $1''$ diameter aperture, FWHM_IMAGE > 2.6 pix, and 50% FLUX_RADIUS > 0 . Following the above procedures results in a “main catalog” of 7538 F160W-detected sources.

We cross-match detections in our catalog with sources in reference catalogs, provided they are within $1''$ of the position returned by SExtractor. To identify LBGs, we use the catalogs produced by Steidel et al. (2003) (hereafter S03) and Mischeva et al. (2017) (hereafter M17). The M17 LBG sample is an expanded version of an LBG sample from Iwata et al. (2009), containing U-dropouts with VLT/VIMOS follow-ups that confirm redshifts $z \geq 3.06$; while this sample overlaps in

part with the Steidel et al. (2003) LBG sample, we keep S03 and M17 LBGs separate in subsequent figures and analysis out of an abundance of caution concerning possible differences in, e.g., color selection criteria. To identify LAEs, we use the catalog from Yamada et al. (2012) and the M17 catalog. We identify AGN based on the X-ray point-source catalog from Lehmer et al. (2009b) and Lyman-continuum (LyC) emitters based on the M17 catalog. For spectroscopic redshifts, if they are not available in one of the aforementioned catalogs, we have taken redshifts from the spectroscopic SSA22 surveys by Saez et al. (2015) and Kubo et al. (2015a), as well as the VLT-VIMOS Deep Survey (VVDS; Le Fèvre et al. 2013). We find spectroscopic redshifts from the above references for 216 of the sources in our catalog. For the subsequent analysis, we require galaxies to have spectroscopic redshifts in order to conclusively identify them as protocluster members or $z \sim 3$ field galaxies. We find that, of these sources, 91 have redshifts $2.9 \leq z \leq 3.3$, with 72 galaxies in the protocluster redshift range ($3.06 \leq z \leq 3.12$), and thus 19 galaxies in the field redshift range. By construction, the M17 LBGs have a spectroscopic redshift; for S03 LBGs, we estimate that our requirement of spectroscopic redshifts may exclude as many as four protocluster LBGs from our subsequent analysis. For additional photometry (covering u^* -band to Spitzer IRAC $8 \mu\text{m}$; see Table 6 for the full list of filters), we have used the photometric catalog of Kubo et al. (2013). We also include narrowband magnitudes at 4972 \AA (the observed wavelength of the Lyman α line at $z = 3.1$) from Yamada et al. (2012), and we report $\log L_X$ (measured from 2–8 keV, approximately 8–32 rest-frame keV) for the X-ray sources in Lehmer et al. (2009b). We estimate that, for the majority of the reference catalogs, the number of possible mismatches with our catalog is on the order of a few galaxies. For the larger Kubo et al. (2013) photometric catalog, the number of mismatches could be as large as 200, though this is still $\sim 11\%$ of the overall number of matches we find with the Kubo et al. (2013) catalog. We note that these numbers of false matches are likely overestimated, since the angular separations of the matches are typically much less than an arcsecond, and there is a large number of sources in our main catalog. Excerpts of the main catalog are provided in Tables 2 and 3 for protocluster LBGs with acceptable fits from GALFITM (as defined in Section 3.1).

In Figure 2, we show how we divide our main catalog into subsamples (based on requirements for spectroscopic redshift, etc.) for the analyses presented in the following sections. Due to the availability of an additional S03 LBG sample in GOODS-N, as well as concerns about how different LBG color selection criteria might harm any protocluster-field comparisons, we focus the majority of the following analysis on the sample of S03 LBGs in our catalog. Our main catalog contains 26 S03 LBGs with $2.9 \leq z \leq 3.3$, to a maximum R -band magnitude of 25.4. These 26 $z \sim 3$ S03 LBGs amount to 13 protocluster LBGs and 13 field LBGs. Our main catalog also contains, in the same redshift range, 13 LBGs that are unique to the M17 catalog; these have a maximum R -band magnitude of 25.5, and amount to 11 protocluster LBGs and 2 field LBGs.

2.3. Comparison LBG Sample in GOODS-N

We constructed an additional comparison sample of LBGs in the GOODS-N field based on the S03 catalog. The S03 GOODS-N catalog contains 40 LBGs with $2.9 \leq z \leq 3.3$, to a maximum R -band magnitude of 25.6. Sérsic parameters for

these galaxies were retrieved by cross-matching with the van der Wel et al. (2012) single-Sérsic fitting catalog. We find that a subset of 33 $z \sim 3$ LBGs have acceptable single-Sérsic fits from van der Wel et al. (2012). We use these Sérsic parameters to increase the size of our field galaxy comparison sample in the analysis described in Section 3.1.

We use UV to mid-IR (U -band to Spitzer MIPS $70 \mu\text{m}$) photometry from the Barro et al. (2019) catalog in the CANDELS survey areas for our comparison LBG sample in GOODS-N, retrieved from the *Rainbow* database.¹² We searched the catalogs for the closest match within $1''$ to each LBG in the Steidel et al. (2003) GOODS-N sample. We estimate that $\lesssim 10$ galaxies could be mismatched with the CANDELS photometric catalog, though this could amount to a significant fraction of the 40 S03 LBGs in GOODS-N. However, we again expect that this number is overestimated, based on the small angular separations between matches. We list the filters used for this photometry in Table 6.

3. Morphological Analysis

3.1. Parametric Morphology Fitting

To analyze the morphologies of our detected galaxies in the SSA22 field, we began by fitting 2D parametric models to the data. The surface brightness profile of an elliptical or spheroidal galaxy without a well-resolved disk is well-described by the Sérsic law, a symmetric profile specified by two parameters, the Sérsic index n and effective radius r_e :

$$I(r) = I_e \exp \left[-b_n \left(\left(\frac{r}{r_e} \right)^{\frac{1}{n}} - 1 \right) \right], \quad (1)$$

where I_e is the surface brightness at $r = r_e$ and b_n satisfies

$$\Gamma(2n) = 2\gamma(2n, b_n), \quad (2)$$

where Γ and γ are the complete and lower incomplete gamma functions, respectively (Graham & Driver 2005). In the general case of an elliptical profile, the r in the equation above is a function of the profile's center and elliptical axis ratio $q = b/a$.

Multiple studies have demonstrated that single-Sérsic model fitting with GALFIT (Peng et al. 2002) can be used to extract galaxy morphologies from large HST data sets (e.g., GEMS (Häussler et al. 2007) and CANDELS (van der Wel et al. 2012)). GALFIT has the ability to deblend nearby sources via simultaneous fitting, allowing accurate photometric measurements in crowded images and the examination of galaxies with close projected companions for evidence of mergers. GALAPAGOS-2 uses GALFITM (Vika et al. 2013) for single-Sérsic model fitting. GALFITM is a modified version of GALFIT, which retains all of the same functionality and runs on the same Levenberg–Marquardt algorithm.

The GALAPAGOS-2 fitting procedure distinguishes between the “primary” source in a cutout, i.e., the main source currently being fit, and “secondary” sources, i.e., nearby objects bright enough to bias the photometry of the primary. For accurate fitting to the primary source, secondary sources must be fit simultaneously. Sources are sorted and fit in order of decreasing brightness, and every source gets a turn as the primary. If a secondary source is present and was already fit (i.e., if the secondary source is brighter than the current

¹² http://rainbowx.fis.ucm.es/Rainbow_navigator_public/

Table 2
Catalog Fits as Defined in Section 3.1, Showing the GALFITM-extracted Morphological Parameters

| ID | S/N ^a | m_{F160W} ^b | δm_{F160W} | r_e ^c (arcsec) | δr_e (arcsec) | n ^d | δn | q ^e | δq | PA ^f (deg) | δ PA (deg) | z ^g | z Src. ^h | Σ_{LAE} ⁱ (arcmin ⁻²) | Vis. Class. ^j | S03 Name ^k |
|---------------------|------------------|--------------------------|--------------------|--------------------------------|--------------------------|------------------|------------|------------------|------------|--------------------------|----------------------|------------------|-----------------------|--|--------------------------|-----------------------|
| J221710.35+001920.8 | 223.5 | 23.50 | 0.07 | 0.09 | 0.03 | 1.15 | 1.41 | 0.45 | 0.22 | 47.76 | 17.56 | 3.103 | M17 | 0.64 | ... | ... |
| J221704.34+002255.8 | 188.2 | 24.80 | 0.32 | 0.18 | 0.11 | 1.28 | 3.04 | 0.72 | 0.52 | -42.55 | 98.42 | 3.108 | M17 | 0.77 | ... | ... |
| J221732.04+001315.6 | 183.6 | 22.93 | 0.06 | 0.32 | 0.03 | 0.65 | 0.17 | 0.78 | 0.06 | 30.23 | 14.57 | 3.065 | M17 | 0.67 | C2 | ... |
| J221737.92+001344.1 | 166.5 | 24.61 | 0.19 | 0.19 | 0.07 | 0.59 | 0.95 | 0.73 | 0.30 | -68.91 | 49.33 | 3.094 | S03a | 1.26 | M2 | SSA22a-MD14 |
| J221731.69+001657.9 | 163.4 | 23.94 | 0.05 | 0.28 | 0.03 | 0.47 | 0.19 | 0.58 | 0.06 | -56.33 | 7.60 | 3.088 | S03a | 0.91 | C2 | SSA22a-M28 |
| J221720.25+001651.7 | 157.0 | 23.32 | 0.06 | 0.38 | 0.03 | 0.82 | 0.18 | 0.73 | 0.06 | -78.20 | 9.94 | 3.098 | S03a | 0.84 | C2 | SSA22a-C35 |
| J221718.87+001816.2 | 156.8 | 24.06 | 0.06 | 0.09 | 0.02 | 1.78 | 1.16 | 0.77 | 0.20 | 12.01 | 32.32 | 3.089 | S03e | 1.20 | M2 | SSA22a-D17 |
| J221718.96+001444.5 | 135.1 | 23.78 | 0.10 | 0.19 | 0.03 | 0.90 | 0.64 | 0.53 | 0.16 | 21.98 | 13.89 | 3.091 | M17 | 0.54 | ... | ... |
| J221701.38+002031.9 | 133.6 | 24.33 | 0.13 | 0.32 | 0.08 | 0.99 | 0.65 | 0.27 | 0.12 | -14.07 | 9.27 | 3.073 | M17 | 0.73 | ... | ... |
| J221720.20+001731.6 | 123.1 | 24.61 | 0.07 | 0.19 | 0.02 | 1.42 | 0.73 | 0.22 | 0.17 | -16.46 | 6.21 | 3.065 | M17 | 1.07 | ... | SSA22a-C47 |
| J221718.04+001735.5 | 120.8 | 24.43 | 0.09 | 0.27 | 0.05 | 1.78 | 1.18 | 0.30 | 0.12 | 31.35 | 7.55 | 3.093 | M17 | 0.86 | ... | ... |
| J221731.51+001631.0 | 118.2 | 24.79 | 0.09 | 0.26 | 0.05 | 0.63 | 0.38 | 0.50 | 0.13 | 56.67 | 11.93 | 3.098 | M17 | 0.88 | ... | SSA22a-M25 |
| J221740.98+001127.2 | 108.7 | 24.28 | 0.10 | 0.21 | 0.04 | 0.95 | 0.66 | 0.32 | 0.16 | 69.28 | 8.14 | 3.093 | M17 | 0.59 | C2 | ... |
| J221719.30+001543.8 | 106.4 | 23.56 | 0.07 | 0.58 | 0.04 | 0.51 | 0.15 | 0.44 | 0.04 | -75.46 | 3.67 | 3.097 | S03a | 0.64 | M3 | SSA22a-C30 |
| J221736.90+001712.8 | 98.1 | 25.08 | 0.08 | 0.29 | 0.04 | 1.17 | 0.51 | 0.24 | 0.09 | 0.22 | 5.07 | 3.099 | M17 | 0.95 | ... | SSA22a-M31 |
| J221721.02+001708.9 | 79.0 | 25.13 | 0.05 | 0.26 | 0.00 | 0.26 | 0.06 | 0.41 | 0.01 | 68.08 | 0.15 | 3.076 | S03e | 1.03 | C2 | SSA22a-C39 |

Notes.^a Signal-to-noise in a 1'' diameter aperture.^b Integrated Sérsic model magnitude.^c Sérsic model effective radius.^d Sérsic model index.^e Sérsic model axis ratio b/a .^f Sérsic model position angle.^g Redshift from literature; see Section 2.2.^h Redshift source: S03e = Steidel et al. (2003) Ly α emission; S03a = Steidel et al. (2003) absorption-line; M17 = Taken from Micheva et al. (2017) catalogs.ⁱ Local LAE surface density; see Section 5.2.^j Consensus visual classification; see Section 3.4.^k S03 catalog designation.

(This table is available in its entirety in machine-readable form.)

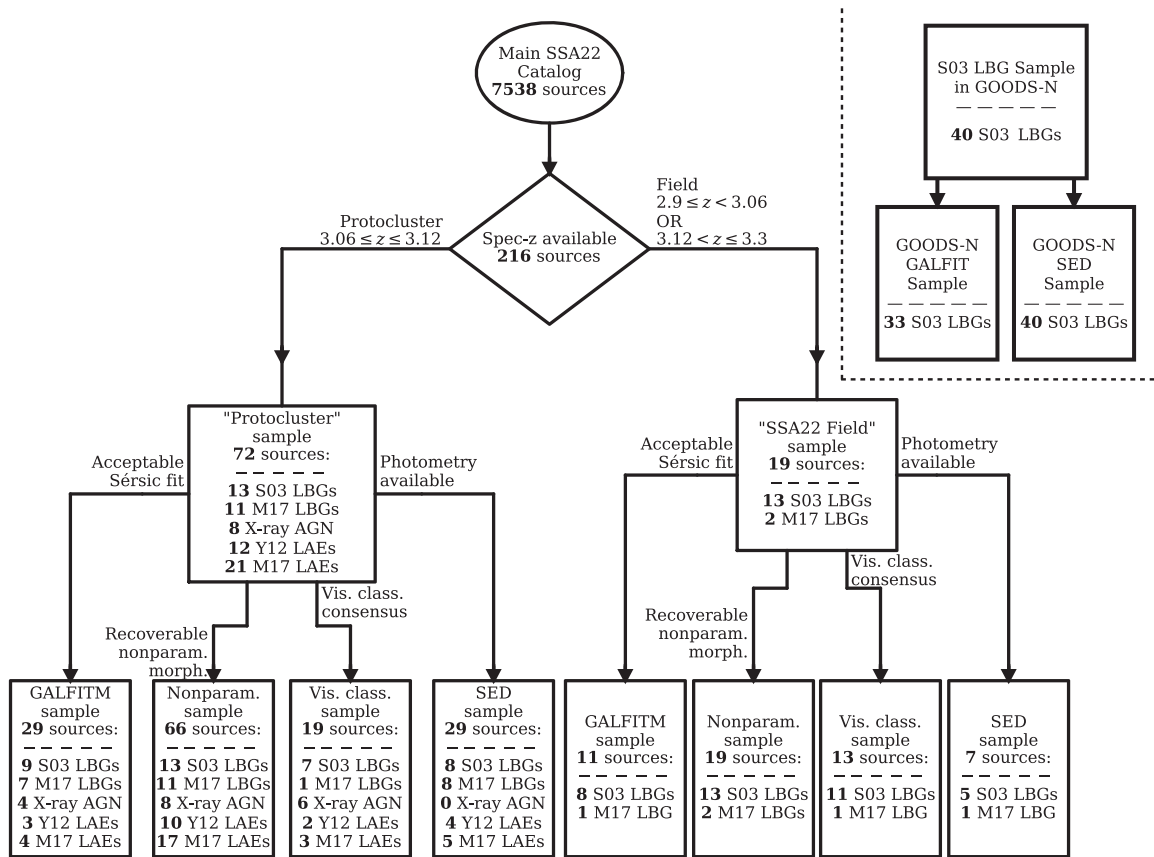


Figure 2. We illustrate how each of the protocluster and field subsamples used throughout this paper stem from the main SSA22 catalog. We require galaxies to have spectroscopic redshifts from the literature, to distinguish between protocluster and field galaxies. To be included in the analysis of our *GALFIT* sample, we require sources to have acceptable Sérsic fits, as defined in Section 3.1. In our analysis of the *nonparametric morphology sample*, we require sources to have a recoverable nonparametric morphology using the procedures described in Section 3.3. In our *visual classification sample*, we include only sources for which our classifiers reached a consensus about whether the system was merging or an isolated galaxy, as described in Section 3.4. Our *SED sample* includes only galaxies for which we could retrieve photometry from the Kubo et al. (2013) photometric catalog. For each subsample, we show the total number of sources as well as the number in different classes and the reference to the classification in the literature. While we focus on the LBG and AGN populations in subsequent sections, we also list the number of LAEs in each sample. We abbreviate the references as: S03—Steidel et al. (2003); Y12—Yamada et al. (2012); M17—Micheva et al. (2017). The X-ray AGN are those studied in Alexander et al. (2016); they are all found in the protocluster, and our SED fitting sample excludes them by construction. Due to the nature of the narrowband LAE selection, there are no field LAEs in our catalog. In the upper right corner, we show the breakdown of our *comparison LBG sample* in *GOODS-N*, made up of 40 *GOODS-N* LBGs from the S03 catalog, 33 of which have acceptable single-Sérsic fits from van der Wel et al. (2012).

Table 3
Catalog Excerpt for Protocluster LBGs with Acceptable Fits as Defined in Section 3.1, Showing Additional Photometry

| ID | u^* | B | | V | R | i' | z' | J | K | $3.6\ \mu\text{m}$ | $4.5\ \mu\text{m}$ | $5.8\ \mu\text{m}$ | $8.0\ \mu\text{m}$ | |
|---------------------|-------|-------|-----|-------|-------|-------|-------|-------|-------|--------------------|--------------------|--------------------|--------------------|-----|
| J221710.35+001920.8 | 26.57 | 25.31 | ... | 24.31 | 24.11 | 23.94 | 23.91 | 23.40 | 22.78 | 23.07 | 23.13 | 22.32 | 23.05 | ... |
| J221704.34+002255.8 | 26.77 | 25.13 | ... | 24.23 | 24.08 | 23.96 | 23.99 | 23.04 | 22.65 | 23.04 | 22.95 | 22.40 | 22.85 | ... |
| J221732.04+001315.6 | 27.61 | 25.66 | ... | 24.49 | 24.16 | 23.85 | 23.85 | 23.26 | 22.34 | 22.11 | 22.02 | 22.12 | 21.49 | ... |
| J221737.92+001344.1 | 26.82 | 26.10 | ... | 25.21 | 24.91 | 24.66 | 24.61 | 24.13 | 23.49 | 23.25 | 23.29 | ... | 22.53 | ... |
| J221731.69+001657.9 | 27.98 | 26.46 | ... | 25.42 | 25.28 | 24.99 | 25.16 | 25.34 | 23.29 | 23.25 | 23.03 | 22.78 | 21.98 | ... |
| J221720.25+001651.7 | 27.57 | 25.80 | ... | 24.83 | 24.56 | 24.36 | 24.36 | 24.16 | 23.18 | 23.63 | 23.69 | 24.76 | 23.27 | ... |
| J221718.87+001816.2 | 26.41 | 25.50 | ... | 24.78 | 24.73 | 24.62 | 24.80 | 24.45 | 24.20 | 23.27 | 23.38 | 22.84 | 21.92 | ... |
| J221718.96+001444.5 | 26.95 | 25.64 | ... | 24.69 | 24.55 | 24.37 | 24.33 | 24.13 | 23.22 | 23.15 | 22.97 | 23.78 | 22.86 | ... |
| J221701.38+002031.9 | 27.50 | 26.68 | ... | 25.43 | 25.08 | 24.78 | 24.78 | 24.58 | 23.01 | 23.30 | 23.01 | 23.29 | 22.29 | ... |
| J221720.20+001731.6 | ... | ... | ... | ... | ... | ... | ... | ... | ... | ... | ... | ... | ... | ... |
| J221718.04+001735.5 | 28.79 | 26.45 | ... | 25.64 | 25.30 | 25.08 | 24.91 | 25.27 | 23.68 | 20.42 | 20.88 | 22.87 | 22.42 | ... |
| J221731.51+001631.0 | ... | ... | ... | ... | ... | ... | ... | ... | ... | ... | ... | ... | ... | ... |
| J221740.98+001127.2 | 26.86 | 26.01 | ... | 25.14 | 24.93 | 24.75 | 24.81 | 23.98 | 23.78 | 23.09 | 23.09 | ... | ... | ... |
| J221719.30+001543.8 | 26.80 | 25.66 | ... | 24.82 | 24.68 | 24.54 | 24.45 | 25.43 | 23.27 | 22.14 | 21.55 | 21.82 | 21.72 | ... |
| J221736.90+001712.8 | ... | ... | ... | ... | ... | ... | ... | ... | ... | ... | ... | ... | ... | ... |
| J221721.02+001708.9 | 27.20 | 26.20 | ... | 25.43 | 25.28 | 25.29 | 25.39 | 24.72 | 23.17 | 24.22 | 24.54 | ... | ... | ... |

Notes. In each column, we show the AB magnitude of the galaxy in the given band, as measured by Kubo et al. (2013). We label the IRAC bands (channel 1–4) by their reference wavelength (3.6–8.0 μm).

primary), the parameters from that fit are reused and held fixed (provided the secondary is in the same image as the primary source; see Figure 9 in Barden et al. 2012). While secondary sources are fit simultaneously, sources that are present in the cutout but are faint enough compared to the primary are not fit, and instead are masked out such that GALFITM ignores any pixels corresponding to these sources. The fit results presented in Table 2 and in what follows represent the primary fit to each source.

Following the generation of the source catalog, GALFITM was used to fit a single Sérsic profile to each F160W detection. We focus on single component fits for individual galaxies, reasoning that, for the $z \sim 3$ we are primarily interested in, bulge-like and disk-like components were unlikely to be resolved separately. The initial guesses and constraints for our fits come from SExtractor parameters. For a given object, the initial guess for the Sérsic model magnitude is the SExtractor MAG_BEST; the initial value for r_e is the 50% FLUX_RADIUS raised to the power of 1.4. The initial value for the Sérsic index is 2.5 for all galaxies, and the initial position of the Sérsic model is the position determined by SExtractor.

GALFIT (and by extension, GALFITM) allows parameter value ranges to be limited and coupled. The following bounds on r_e , n , and the Sérsic profile magnitude m were adopted for this work:

$$\begin{aligned} 0''.002 < r_e < 26''; \\ 0.2 < n < 10; \\ |m_{SE} - m| < 5, \end{aligned}$$

where m_{SE} is the magnitude reported by SExtractor. In pixel units, the constraint on Sérsic radius is $0.3 < r_e < 400$, where the lower limit is hard-coded into GALAPAGOS-2. These constraints are a slight relaxation of the GALAPAGOS-2 defaults, which are themselves selected to do a good job of keeping the fit from wandering into unphysical regions of the parameter space without being overly restrictive. The center of the model is constrained so that it can only move within 10% of the cutout size from the initial position.

Following van der Wel et al. (2012), we flagged fits where the primary fit is unlikely to represent the galaxy well as unacceptable, based on the following criteria. We flagged fits where any of the final parameter values were equal to one of the bounds listed above and fits where the final Sérsic index was equal to the initial value of 2.5 as unacceptable. The GALFIT algorithm occasionally converges on an arbitrarily small axis ratio for low-S/N objects with small apparent sizes. For this reason, we also flagged fits with axis ratios less than 0.125. Apparently well-converged fits that do not represent the data well also have exceptionally large errors in the resulting total Sérsic magnitude and effective radius, so we flagged fits where the magnitude error estimated by GALFITM is greater than 5 mag (more typical errors are on the order of 0.08 mag for acceptable fits and 1.4 mag for unacceptable fits), and we also flagged fits where the recovered effective radius was consistent with 0 within 1σ .

Of our main catalog, 2833 detections (37.6% of detections) have acceptable single-Sérsic fits according to the criteria above. Sources with acceptable fits tend to be brighter and have larger effective sizes than sources with bad fits; foreground stars and other point-like sources tend to have bad fits, as do faint, compact galaxies like LAEs. In terms of SExtractor parameters, poorly fit sources tend to have $23.5 \leq \text{MAG_BEST} \leq 26.1$ and (in

pixel units) $4.41 \leq \text{FWHM_IMAGE} \leq 9.84$; sources with acceptable fits tend to have $21.9 \leq \text{MAG_BEST} \leq 24.7$ and $5.71 \leq \text{FWHM_IMAGE} \leq 13.25$. The fraction of acceptable fits increases slightly among sources with $2.9 \leq z \leq 3.3$: 40 (44.0%) have acceptable Sérsic fits. In Figure 2, we show how the sources with acceptable fits break down between the protocluster and field, along with the numbers of LBGs and other categories of galaxies with acceptable fits. Among the sources with acceptable fits, we identify 29 spectroscopically confirmed protocluster members, nine of which are LBGs from the S03 catalog and seven of which are LBGs exclusive to the M17 catalog. Only four of the eight X-ray detected protocluster AGN from Lehmer et al. (2009b) have acceptable Sérsic fits under the criteria above; the fits to the rest-frame optically bright AGN (e.g., the quasar SSA22a-D12) do not return especially meaningful or well-constrained Sérsic model parameters, due to their point source-like profiles.

We present the parameters derived from model fitting in Figure 3; to broaden the field galaxy comparison sample, we include single-Sérsic-fit parameters from the 33 galaxies in our GOODS-N comparison sample with good fits from van der Wel et al. (2012) (see Section 2.3) in the figure.

To assess whether or not the morphologies of the protocluster and field samples are drawn from the same underlying population, we use 1D and 2D two-sample Kolmogorov–Smirnov (hereafter, KS) tests, under the null hypothesis that the results for the protocluster and field samples are drawn from the same distribution. For a fair comparison between LBGs selected by the same color criteria, we initially limited the tests to S03 LBGs. The tests are consistent with the null hypothesis that the S03 protocluster and S03 field LBGs are drawn from the same morphological population. We then performed the same KS tests with the addition of the M17 LBGs, finding again that all the tests on the parametric morphologies are consistent with the null hypothesis. We show the results for both sets of 1D and 2D KS tests in Table 4.

We note that the one-to-two orbit depth of our images is not ideal for parametric model fitting; however, in Appendix A we use simulated galaxies similar to our LBG sample to investigate how decreasing S/N affects the reliability of our fits. We find that the fits are generally reliable for low- n galaxies with $S/N \gtrsim 100$. Noting that only two galaxies in Table 2 fall below this rough threshold and that their Sérsic model parameters appear well constrained according to the error estimates from GALFITM, we are confident in the reliability of the fits to the LBG samples we use above.

In hierarchical models, galaxies with bulge-dominated early-type morphologies are assembled by past mergers. More evolved galaxies that have experienced a number of past mergers should then have larger Sérsic indices. Since we probe a young population by relying on a Lyman-break-selected sample, larger-than-expected Sérsic indices could be an indication of more rapid, merger-driven morphological evolution. We note that the majority of our LBGs have more disk-like morphologies with $n < 2.5$, and all of the protocluster LBGs fall below this line. The protocluster LBGs do not tend to have larger n than field galaxies, nor do they tend to be larger, suggesting that the morphologies of LBGs in the protocluster are not evolving faster than their field counterparts at $z \sim 3$. We note that in Appendix A we find that our Sérsic model fits typically recover n smaller than the “true” value of n due to the broadening effects of the PSF on the Sérsic model. For the four protocluster LBGs with recovered Sérsic indices

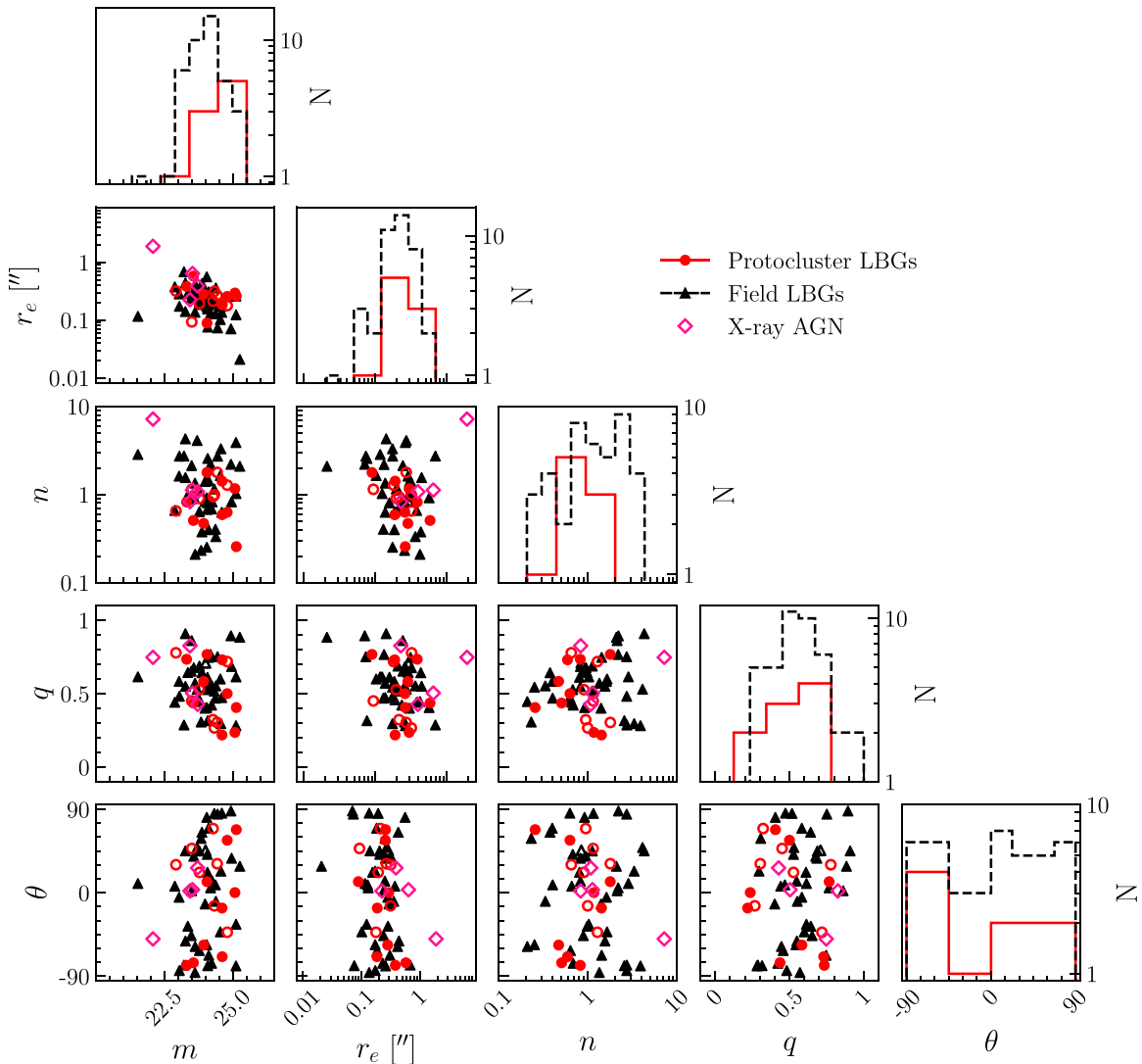


Figure 3. On the diagonal, we show the distributions of Sérsic fit parameters—integrated F160W magnitude m , effective radius r_e , Sérsic index n , axis ratio q , and position angle θ —for the S03 LBGs with acceptable fits in the final SSA22 catalog and the comparison GOODS-N sample with fits from van der Wel et al. (2012). Off-diagonal, we show correlations between the parameters for S03 LBGs, M17 LBGs, and protocluster AGN with acceptable fits. We show LBGs associated with the protocluster ($3.06 \leq z \leq 3.12$) in red (circles, solid lines), and field LBGs in black (triangles, dashed lines). While the histograms on the diagonal are limited to only S03 LBGs, on the off-diagonal scatter plots we show both S03 LBGs (filled symbols) and M17 LBGs (open symbols). The X-ray detected protocluster AGN are shown on the scatter plots as open magenta diamonds.

$1.25 < n < 2$, we thus expect that the true Sérsic index could be as much as a factor of 2 larger in the case of $S/N \gtrsim 100$, possibly indicating an underlying bulge-dominated morphology smeared out by the effects of the PSF. However, we note that the PSF also affects the field LBGs, and given again that the protocluster and field LBGs cluster together strongly in the space of the Sérsic model parameters, we are confident in assessing that the protocluster LBGs are not more morphologically evolved than the field LBGs.

3.2. Residual Image Analysis

For the subset of 25 SSA22 LBGs (16 protocluster and 9 field) in our sample with acceptable fits, we show the residuals after model subtraction in Figures 4 and 5 for protocluster and field galaxies, respectively. We used the Python-based tidal feature extraction pipeline¹³ from Mantha et al. (2019) to

examine our single-Sérsic fit residuals for evidence of potential tidal features related to recent mergers. Briefly, the Mantha et al. (2019) method identifies flux- and area-wise significant contiguous pixel regions in residual images. We set the pipeline to search for connected regions of pixels $\geq 2\sigma$ above the background after convolution with a boxcar filter 3 pixels wide. Based on the average galaxy size at $z \sim 3$, we searched for residual features within 15 kpc of the main galaxy. To ensure that undersubtracted regions at the center of a galaxy were not erroneously detected as possible tidal features, we also set the pipeline to mask out an ellipse centered on the source position, which has major and minor axes scaled up 2.5 times from the SExtractor detection ellipse. Additionally, since the goal of the pipeline is to extract low surface brightness features associated with mergers, bright features are masked in the image before extraction, in order to exclude bright companion galaxies from being identified as tidal features.

Three galaxies in our LBG sample are deliberately excluded from this analysis: J221732.04+001315.6, a protocluster LBG,

¹³ https://github.com/AgentM-GEG/residual_feature_extraction

Table 4
One- and Two-dimensional KS Test Statistics and Probabilities for Derived Properties and Correlations of Protocluster and Field LBGs

| Protocluster/Field Comparison | S03 LBGs ^a | | | | S03 and M17 LBGs ^b | | | |
|-------------------------------|-----------------------|----------------------|-------------------|-------------------|-------------------------------|--------------------|-----------------|-----------------|
| | N_{proto}^c | N_{field}^d | D_{KS}^e | p_{KS}^f | N_{proto} | N_{field} | D_{KS} | p_{KS} |
| m | 9 | 41 | 0.43 | 0.09 | 16 | 42 | 0.28 | 0.28 |
| $\log r_e$ | 9 | 41 | 0.30 | 0.41 | 16 | 42 | 0.26 | 0.37 |
| $\log n$ | 9 | 41 | 0.36 | 0.23 | 16 | 42 | 0.31 | 0.17 |
| q | 9 | 41 | 0.25 | 0.66 | 16 | 42 | 0.27 | 0.31 |
| G | 13 | 13 | 0.54 | 0.04 | 24 | 15 | 0.32 | 0.25 |
| M_{20} | 13 | 13 | 0.38 | 0.30 | 24 | 15 | 0.28 | 0.41 |
| C | 13 | 13 | 0.38 | 0.30 | 24 | 15 | 0.23 | 0.61 |
| M_* | 8 | 45 | 0.58 | 0.01 | 15 | 46 | 0.58 | 0.00 |
| SFR | 8 | 45 | 0.49 | 0.05 | 15 | 46 | 0.54 | 0.00 |
| sSFR | 8 | 45 | 0.24 | 0.75 | 15 | 46 | 0.22 | 0.57 |
| Mass-weighted age | 8 | 45 | 0.23 | 0.80 | 15 | 46 | 0.19 | 0.75 |
| Joint Distribution Tests | | | | | | | | |
| $m - \log r_e$ | 9 | 41 | 0.28 | 0.59 | 14 | 42 | 0.26 | 0.42 |
| $m - \log n$ | 9 | 41 | 0.40 | 0.20 | 14 | 42 | 0.28 | 0.32 |
| $m - q$ | 9 | 41 | 0.43 | 0.12 | 14 | 42 | 0.26 | 0.40 |
| $\log r_e - \log n$ | 9 | 41 | 0.32 | 0.44 | 14 | 42 | 0.26 | 0.40 |
| $\log r_e - q$ | 9 | 41 | 0.29 | 0.55 | 14 | 42 | 0.25 | 0.45 |
| $\log n - q$ | 9 | 41 | 0.36 | 0.30 | 14 | 42 | 0.29 | 0.29 |
| $G - M_{20}$ | 13 | 13 | 0.54 | 0.05 | 24 | 15 | 0.40 | 0.10 |
| $C - M_{20}$ | 13 | 13 | 0.46 | 0.13 | 24 | 15 | 0.32 | 0.28 |
| $G - C$ | 13 | 13 | 0.54 | 0.05 | 24 | 15 | 0.40 | 0.10 |

Notes. For tests on parametric morphological properties and physical properties, we include galaxies from our comparison sample of GOODS-N field LBGs. For the physical properties, we show only the results for the SED fits with $Z = 0.655Z_{\odot}$; the results of the tests are not significantly different for the fits with $Z = Z_{\odot}$. We exclude the M17 LBG J221718.04+001735.5 from the KS tests on the SED-fitting derived parameters, due to likely contamination of its near-IR photometry by a nearby point source.

^a Comparing protocluster and field LBGs from the S03 catalog only.

^b Comparing protocluster and field LBGs from both the S03 and M17 catalogs.

^c Number of protocluster LBGs in comparison.

^d Number of field LBGs in comparison.

^e Two-sample KS test statistic.

^f Two-sample KS test p -value.

which appears to be 2–3 sources blended within 5 kpc, and both J221717.69+001900.3 and J221717.68+001901.0 (SSA22a-M38), a pair of field LBGs that are also blended together within 5 kpc, though they were detected and fit separately by our GALAPAGOS-2 pipeline. We excluded these blended galaxies even though they may be merging systems that are physically associated. In such close associates, the blending makes it difficult to reliably fit and mask the images in a way that prevents the pipeline from extracting underfitted components of the blended system as tidal features.

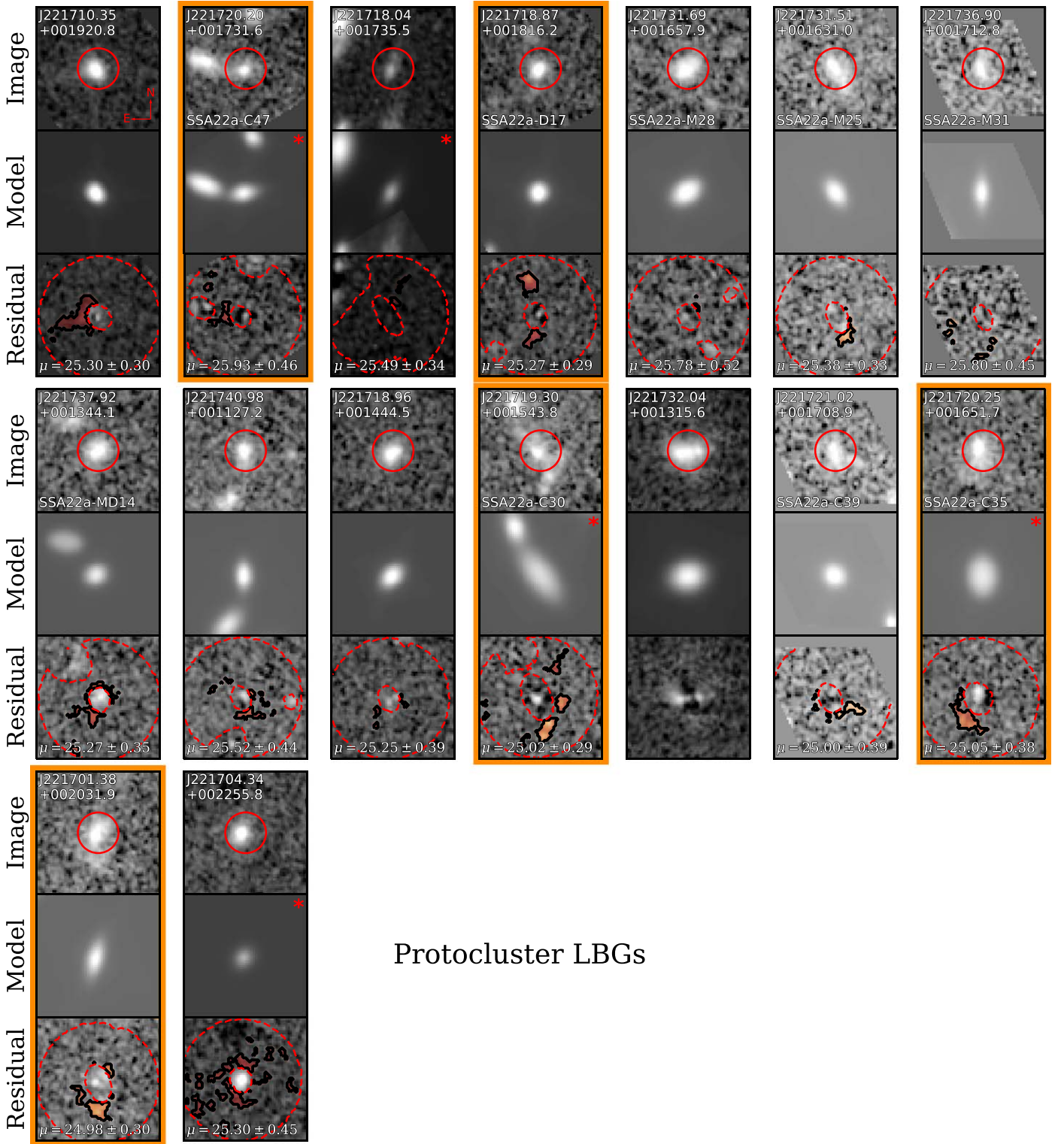
To ensure the cleanest possible residuals, we refit the “original” models from the GALAPAGOS-2 pipeline for five galaxies with small adjustments to improve their positioning. For instance, the fitting cutout for J221718.04+001735.5 contains a bright, unrelated point source that was originally poorly fit with a Sérsic model and adversely affected the positioning of the other models in the image. We fit this cutout again, with the point source properly modeled by a PSF, and allow the positions of the other models to vary. We also found that secondary galaxies in the cutouts containing J221720.20+001731.6 (SSA22a-C47) and J221719.30+001543.8 (SSA22a-C30) were undersubtracted due to offsets in the positions of their models; we refit them with the magnitude and

shape parameters fixed, and the position parameters allowed to vary.

In the case of both J221720.25+001651.7 (SSA22a-C35) and J221704.34+002255.8, the main concentration of the galaxy appears offset from the center of the original GALAPAGOS-2 pipeline model, which is fit to both the concentrated component and an apparent fainter, diffuse component that extends asymmetrically to the southeast of the main concentration. To recenter the fit on the dominant, concentrated feature, we computed the centroid of the pixels $\geq 4\sigma$ above the background and refit the cutout with the primary model fixed to that position. The best-fit model parameters of the primary galaxy do not change significantly in any of these cases, except for the position of the fits to SSA22a-C35 and J221704.34+002255.8, by construction.

We show the features extracted by the tidal feature pipeline in the residual panels of Figures 4 and 5, along with their surface brightness in mag arcsec^{-2} and the unmasked area in which they were extracted.

The extracted features are all of low surface brightness. The range of 2σ limiting surface brightness in our two-orbit images is 25.0–25.4 mag arcsec^{-2} ; in the single-orbit images the range is 24.6–25.1 mag arcsec^{-2} . In terms of surface brightness alone, none of the extracted features are unambiguous; only



Protocluster LBGs

Figure 4. SSA22 protocluster LBGs in our sample with acceptable single-Sérsic fits. We display the original F160W image, model, and residual at the same normalization and stretch for each galaxy. In four cases, we have refit the model with adjustments to the position of the models in order to allow for cleaner tidal feature extraction; we mark these cases with a red star in the model panel. The red circle shows a 10 proper kpc diameter aperture at the position of the primary source. In the top-left corner of each F160W cutout, we print the galaxy’s J2000 positional identifier; for LBGs in the S03 catalog, we print their catalog designation in the lower left corner. In the residual panel, we highlight features extracted by the tidal feature pipeline in an orange colormap and print the surface brightness of the extracted features in mag arcsec⁻². The regions inside the inner dashed red line and outside the outer dashed red line were excluded from feature extraction. Image blocks for galaxies where we have found a plausible tidal feature are outlined with a thick orange border.

four galaxies have extracted features with surface brightness brighter than the 2σ limit: J221710.35+001920.8, J221718.87+001816.2 (SSA22a-D17), J221719.30+001543.8 (SSA22a-

C30), and J221701.38+002031.9. While the surface brightnesses of the features in the other galaxies are on the order of the limiting surface brightness, the sizes of the features in most

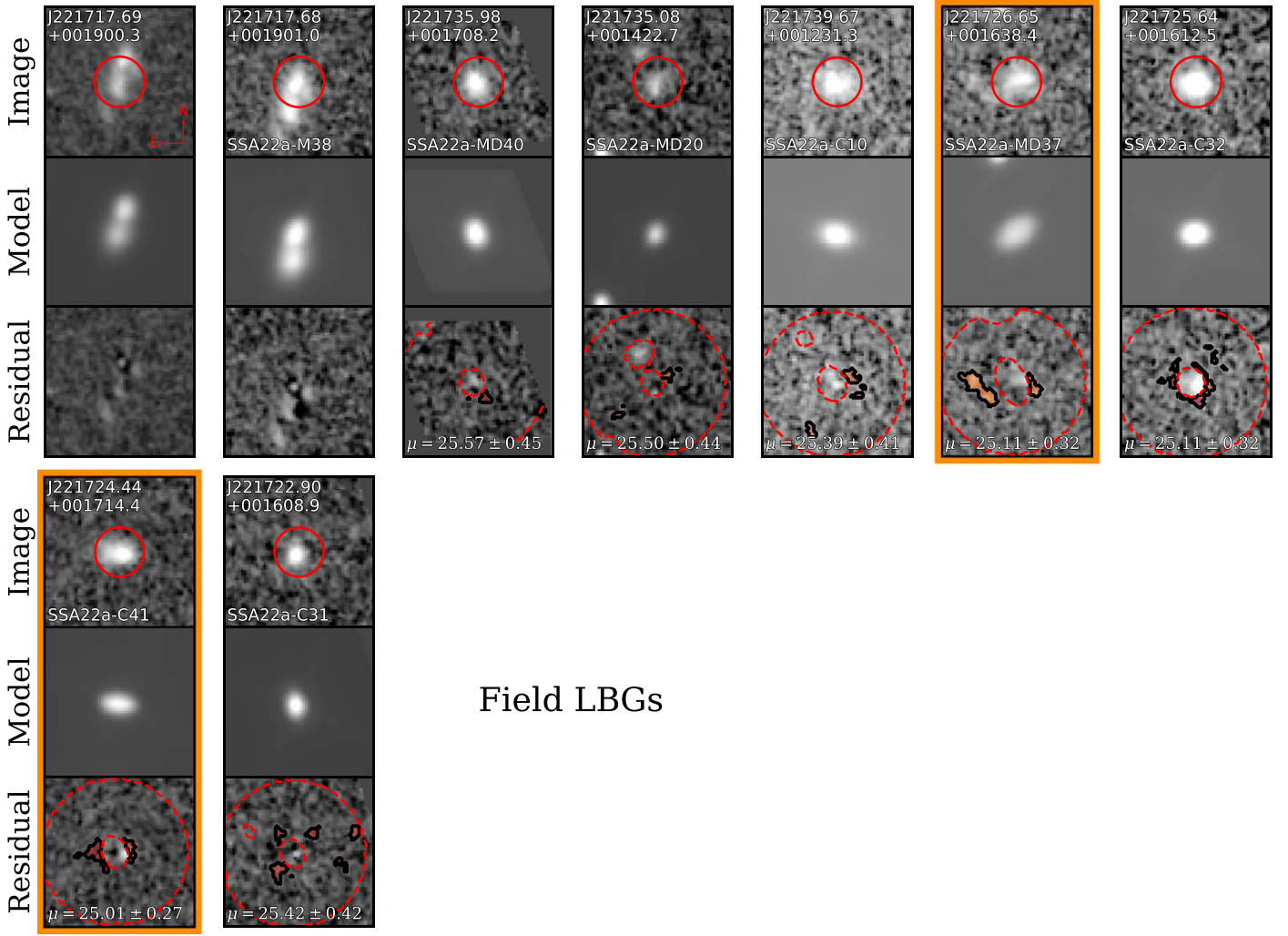


Figure 5. SSA22 field LBGs in our sample with acceptable single-Sérsic fits. All annotations are the same as Figure 4.

cutouts indicate that they are unlikely to be due to noise alone. In one case, J221731.69+001657.9 (SSA22a-M28), the area of the largest residual feature is small enough to be consistent with noise, and we thus exclude the extracted features in this galaxy cutout from consideration as plausible tidal features; in the remainder of cases, we estimate a probability $p < 0.02$ that the largest feature is due to noise, based on simulations of the image background. In classifying residual features as plausible tidal features resulting from merger activity, we focus on three additional criteria: (1) asymmetry with respect to the primary galaxy, (2) extension, and (3) plausible physical association with the primary galaxy. As a rule of thumb, we consider features that reach within 5 kpc of the primary galaxy’s center to plausibly be physically associated with the galaxy.

While the residual feature in the J221710.35+001920.8 cutout is extended, asymmetric, and plausibly associated with the main galaxy, we note that it is positioned near the expected location of a diffraction spike from the WFC3 PSF. Though the extracted feature has low surface brightness, the galaxy is very concentrated in appearance, and the Sérsic model fit is concentrated and visibly PSF-like in appearance. For these reasons, we do not consider the feature extracted from the J221710.35+001920.8 cutout to be plausibly tidal.

Two features are extracted in the SSA22a-D17 cutout, associated with clumpy features to the north and south of the main galaxy in the original image. The features are asymmetrical in size and shape, and both are within 5–10 kpc of the model barycenter. The residual features in the SSA22a-C30 cutout are also associated with clumpy structures that are apparent in the original image, to the southwest of the main galaxy. These clumpy features are also asymmetrical with respect to the main galaxy, and extend between 5 and 10 kpc away from the primary model’s barycenter. Similar clumpy residual features have been observed by Mantha et al. (2019) in mock two-orbit F160W observations of merging galaxies in the VELA cosmological simulations (Ceverino et al. 2014; Zolotov et al. 2015). The simulated observations suggest that similar features may be associated with the late stages of a major merger (i.e., 0.15–0.80 Gyr after the galaxies coalesce), when multiple nuclei are no longer apparent (see Figure 9 in Mantha et al. 2019). The feature extracted in the J221701.38+002031.9 cutout is brighter than the limiting surface brightness in the image, and appears to be asymmetrical and plausibly physically associated with the galaxy. Its shape and offset from the main concentration of the galaxy suggest that it may be tidal in origin, though this galaxy is in a single-orbit image. We are thus less confident in assessing this as a plausible tidal feature.

The apparent association of the small residual feature in the SSA22a-C47 cutout with both galaxies may suggest interaction; residual features bridging the two galaxies seem to be common in mergers (see, e.g., Figures 7 and 9 in Mantha et al. 2019). If these two galaxies are at the same redshift, they might then be a pre-coalescence merging pair, based on the residual feature and the apparent bridge between the galaxies in the original image. However, we have not found a spectroscopic redshift in the literature for the projected companion galaxy, nor do we have independent photometric redshifts for both galaxies, so we are unable to establish whether the apparent companion is physically close to the primary galaxy.

The irregularly shaped galaxy SSA22a-C35 has a diffuse feature offset to the southeast from the main concentration of the galaxy, with a surface brightness of $\approx 25 \text{ mag arcsec}^{-2}$. This feature, based on its shape and plausible physical association with the galaxy, may also be associated with the late, post-coalescence stages of a merger. However, the data we used to fit this galaxy was taken at single-orbit depth, and the quality of the fit is poor. We are thus less confident in assessing this as a plausible tidal feature.

Based on the above, we find 2–5 residual features that may plausibly be tidal in our protocluster LBGs. The clumpy features associated with SSA22a-D17 and SSA22a-C30 are the most plausible, and the diffuse features associated with SSA22a-C35 and J221701.38+002031.9 are the least plausible. If we extrapolate this to a merger fraction based on the number of S03 LBGs we applied the pipeline to, we find a protocluster LBG merger fraction of 0.22–0.44, comparable to the merger fraction we derive by naïve visual classification of S03 LBGs in Section 3.4. If we include M17 LBGs, we find a protocluster merger fraction of 0.13–0.33.

Of the seven field LBGs we have applied the pipeline to, J221735.08+001422.7 (SSA22a-MD20), J221726.65+001638.4 (SSA22a-MD37), and J221724.44+001714.4 (SSA22a-C41) have offset features apparent in the original image, though the feature near SSA22a-MD20 is bright enough to be masked by the residual extraction pipeline. For consistency with the above, we consider only the features near SSA22a-MD37 and SSA22a-C41. These features are both consistent with the 2σ limiting surface brightness in their respective images. Both features are asymmetric and plausibly physically associated with the galaxy, though the feature in the SSA22a-C41 cutout is smaller and closer to the main concentration of the galaxy. We note the superficial similarities of the extracted features in the SSA22a-MD37 cutout to the clumpy features associated with SSA22a-D17 and SSA22a-C30, and conclude that they may be tidal features. The feature in the SSA22a-C41 cutout is more ambiguous; in the original image, it appears that the galaxy is asymmetric, with the eastern side of the galaxy being fainter and more diffuse. The extracted feature is apparently associated with this diffuse region of the main galaxy, similar to SSA22a-C35 above, but smaller in size. We thus find this to be a low-confidence tidal feature, as with SSA22a-C35. Based on the seven field LBGs we applied the pipeline to, we find a field merger fraction of 0.14–0.28, comparable to the protocluster merger fraction we found above, and the merger fractions derived by visual classification in Section 3.4.

We note that conclusive or completely quantitative identification of residual features as being due to mergers is beyond the scope of this work. The relationship between the observed strength and shape of tidal features and the different stages of a merger is not yet fully explored, and will require comprehensive

simulations to establish. Thus, rather than attempting to conclusively identify mergers with this technique, we have classified features only as “plausibly” tidal above, and we treat this method as a supplement to the more established methods of morphological analysis we use in the other sections of this paper.

To roughly estimate the mass of the plausible tidal features above, we used the protocluster and field SED models described in Section 4 to calculate mass-to-light ratios in the F160W band. We find $M/L = 0.45 M_{\odot}/L_{\odot}$ for the protocluster model and $M/L = 0.22 M_{\odot}/L_{\odot}$ for the field model, both assuming $z = 3.1$. These are in agreement with rest-frame B –band mass-to-light ratios calculated from the models using the $B - R$ color relationship in Zibetti et al. (2009, see their Appendix B). Using the F160W mass-to-light ratios we derived, we find that the plausible tidal features associated with the protocluster galaxies have masses on the order of $10^9 M_{\odot}$, ranging from $\log_{10} M_{\star}/M_{\odot} = 9.10$ to 9.78, suggesting that the largest of the clumps have masses comparable to the Small Magellanic Cloud. Assuming a typical stellar mass of $10^{10} M_{\odot}$ for protocluster LBGs (see Figure 8) we find feature mass to total stellar mass ratios ranging from 0.13 to 0.60. These feature mass ratios, along with the compact or clumpy nature of some of the residuals (e.g., SSA22a-C30), suggest that this technique may be sensitive to minor mergers (mass ratio < 0.25), and that some of the features we extract may be infalling satellite galaxies.

3.3. Nonparametric Morphological Analysis

To mitigate the limits imposed by requiring well-converged Sérsic fits to our data, we also pursued nonparametric morphological analysis. We applied this analysis to the $z \sim 3$ SSA22 S03 and M17 LBGs in our sample, excluding LBGs from the GOODS-N comparison sample. The Gini coefficient G of a galaxy’s flux (Abraham et al. 2003) and the second-order moment of light statistic M_{20} for the brightest 20% of light from a galaxy (Lotz et al. 2004) can be used in concert to identify merger candidates. We used the definition of G from Lotz et al. (2004):

$$G = \frac{1}{\overline{|f|}n(n-1)} \sum_i^n (2i - n - 1)|f_i|, \quad (3)$$

where $\{|f_i|\}$ contains the absolute values of the source flux, sorted from smallest to largest, and $\overline{|f|}$ denotes the mean of these values. The Gini coefficient describes the equality of the distribution of light in a galaxy, with values close to 0 indicating an egalitarian distribution of flux and values approaching 1 indicating an unequal distribution.

The total second-order moment of light is defined as

$$M_{\text{tot}} = \sum_i^n f_i r_i^2 = \sum_i^n f_i [(x_i - x_c)^2 + (y_i - y_c)^2], \quad (4)$$

where r_i is the distance from the pixel containing flux f_i to the center (x_c, y_c) of the galaxy; in this context, the center is defined as the location that minimizes M_{tot} . M_{20} is then computed as

$$M_{20} = \log_{10} \left(\frac{\sum_j^n f_j r_j^2}{M_{\text{tot}}} \right), \quad (5)$$

where m is the largest index satisfying

$$\sum_j^m f_j \leq 0.2f_{\text{tot}} \quad (6)$$

when $\{f_j\}$ contains the flux of the pixels sorted from largest to smallest. Values of M_{20} close to 0 indicate excesses of flux further from the galactic centers, which may indicate star-forming knots, multiple nuclei, or otherwise disturbed morphologies. Smaller (more negative) values indicate concentration of light at the center of the galaxy; local quiescent elliptical galaxies have average $M_{20} \sim -2.5$, for example (Lotz et al. 2004).

Locally, the difference between mergers and “normal” galaxies is well-established in the Gini- M_{20} plane; disturbed morphologies create an unequal, off-center distribution of light, so mergers tend to fall above the Gini- M_{20} trend—canonically, the line $G = -0.14M_{20} + 0.33$ (Lotz et al. 2008)—with larger values of M_{20} , while normal galaxies fall below. The Gini coefficient is expected to remain relatively unbiased at $z \gtrsim 2$, given high S/N and resolution better than 500 proper pc pixel⁻¹; M_{20} may be biased by the flattening of the angular size of features at high redshift, though its large dynamic range may still prove useful in distinguishing between disturbed and undisturbed morphologies (Lotz et al. 2004). The physical resolution of our images is 496 proper pc pixel⁻¹ at $z = 3.09$, approaching the limit of what Lotz et al. (2004) recommend. In Appendix A, we used simulations of galaxies similar to our LBG sample to investigate how G , M_{20} , and C are biased by decreasing S/N, finding that they are relatively stable over the range of S/N in our sample.

As a nonparametric analog to the Sérsic index, we also calculated the concentration parameter C , defined as

$$C = 5 \log \left(\frac{r_{80}}{r_{20}} \right), \quad (7)$$

where r_{80} and r_{20} are the radii enclosing 80% and 20% of the total flux, respectively (Conselice et al. 2003). Here, the total flux is defined as the flux contained within 1.5 Petrosian radii. The value of C tends to increase for more concentrated, bulge-dominated morphologies (i.e., with increasing n).

We adopted a method similar to that of Lotz et al. (2004) to compute G , M_{20} , and C . We defined a new segmentation map for each detection by first computing its elliptical Petrosian radius r_p . We then smoothed the image of the galaxy with a Gaussian with $\sigma = r_p/5$, measured the mean flux $\mu(r_p)$ of the pixels at r_p , and assigned any pixels with flux greater than $\mu(r_p)$ to the new segmentation map. Finally, we computed G and M_{20} for each detection using all the pixels included in this new segmentation map. It is possible for this process to fail if, for example, the Petrosian radius cannot be computed or the new segmentation map contains multiple disjoint features. In these cases (6 of the 72 galaxies with protocluster redshifts, all of which are LAEs), we do not report G , M_{20} , or C in the catalog. However, we were able to recover all three quantities for all of the protocluster and field LBGs in our F160W images, as well as the eight protocluster AGN in our images.

We show the derived values of G , M_{20} , and C for protocluster and SSA22 field LBGs in Figure 6. Both S03 protocluster and SSA22 field LBGs cluster together with median (G , M_{20} , C) of (0.37, -1.26 , 2.15) and (0.44, -1.52 , 2.25), respectively. While most of the X-ray AGN fall in the

same area of G - M_{20} space as our LBG samples, they tend to be more concentrated than normal galaxies, falling mainly to the upper right of the trend in G - C space, as expected in cases where the AGN dominates the rest-frame optical emission from the galaxy.

In Figure 6, we adopt the G - M_{20} classifications from Lotz et al. (2008), which show that galaxies with $G > -0.14M_{20} + 0.33$ are merger-like and galaxies with $G \leq -0.14M_{20} + 0.33$ and $G > 0.14M_{20} + 0.80$ are bulge-dominated (i.e., Hubble classes E, S0, and Sa). The majority of our galaxies occupy the third region defined by these two lines, where galaxies with irregular and disk-dominated morphologies (i.e., Hubble classes Sb, Sc, and Ir) fall at low redshift. However, there is significant concern about the use of cuts in the G - M_{20} plane to classify mergers at high redshift. Artificial redshifting of simulated merging systems suggests that the typical G - M_{20} criteria may miss a significant number of mergers at high redshift, and that any apparent trend toward the merger-like region of the G - M_{20} plane may only be a function of mass (Abruzzo et al. 2018). Snyder et al. (2015) also find that the joint distribution of G and M_{20} is narrow at $z \sim 3$, even for diverse morphological types, due to the G - M_{20} segmentation algorithm excluding the low surface brightness outer regions of the galaxy. As such, mergers without clear-cut cases of multiple nuclei may not separate from normal galaxies in the G - M_{20} plane.

It is also apparent from our analysis that the G - M_{20} criteria might miss mergers: the systems in which we see plausible tidal features in Section 3.2 do not all fall above the merger-like/disk-like dividing line in Figure 6, nor do the galaxies visually classified as mergers in Section 3.4. Only two galaxies fall in the merger region: J221740.98+001127.2, an M17 protocluster LBG, and J221726.65+001638.4 (SSA22a-MD37) an S03 field LBG. Neither of these galaxies has obvious multinuclear structure; rather, their elevated G and M_{20} values appear to be due to diffuse, asymmetric features that extend away from the main concentration of the galaxy. As we have noted in Section 3.2, such features could be tidal structures associated with the late stages of a merger. In Section 3.2, we identified clumpy structures associated with SSA22a-MD37, though we found no significant residual features associated with J221740.98+001127.2. Given this inconsistency, and the fact that other galaxies in which we have identified plausible tidal features do not have G and M_{20} values consistent with the Lotz et al. (2008) merger classification, we hesitate to draw any conclusions about the SSA22 protocluster merger fraction from the G - M_{20} classification.

Protocluster LBGs also do not appear to be more morphologically evolved, or bulge-like, by the Lotz et al. (2008) criteria, though given that the merger criterion evidently misses mergers, we cannot conclusively apply the bulge criterion here. Additionally, the protocluster and field LBGs cluster along the same locus in the G - C plane, with neither set of galaxies conclusively being more concentrated or bulge-dominated than the other.

Beyond using G and M_{20} to attempt to classify mergers, we also attempted to use them to distinguish between the protocluster and field populations. We show 1D and 2D KS test results for the individual and joint distributions of nonparametric morphologies in Table 4. We again limited these tests to S03 LBGs, but here we are restricted to the protocluster and the SSA22 field. The KS test results for

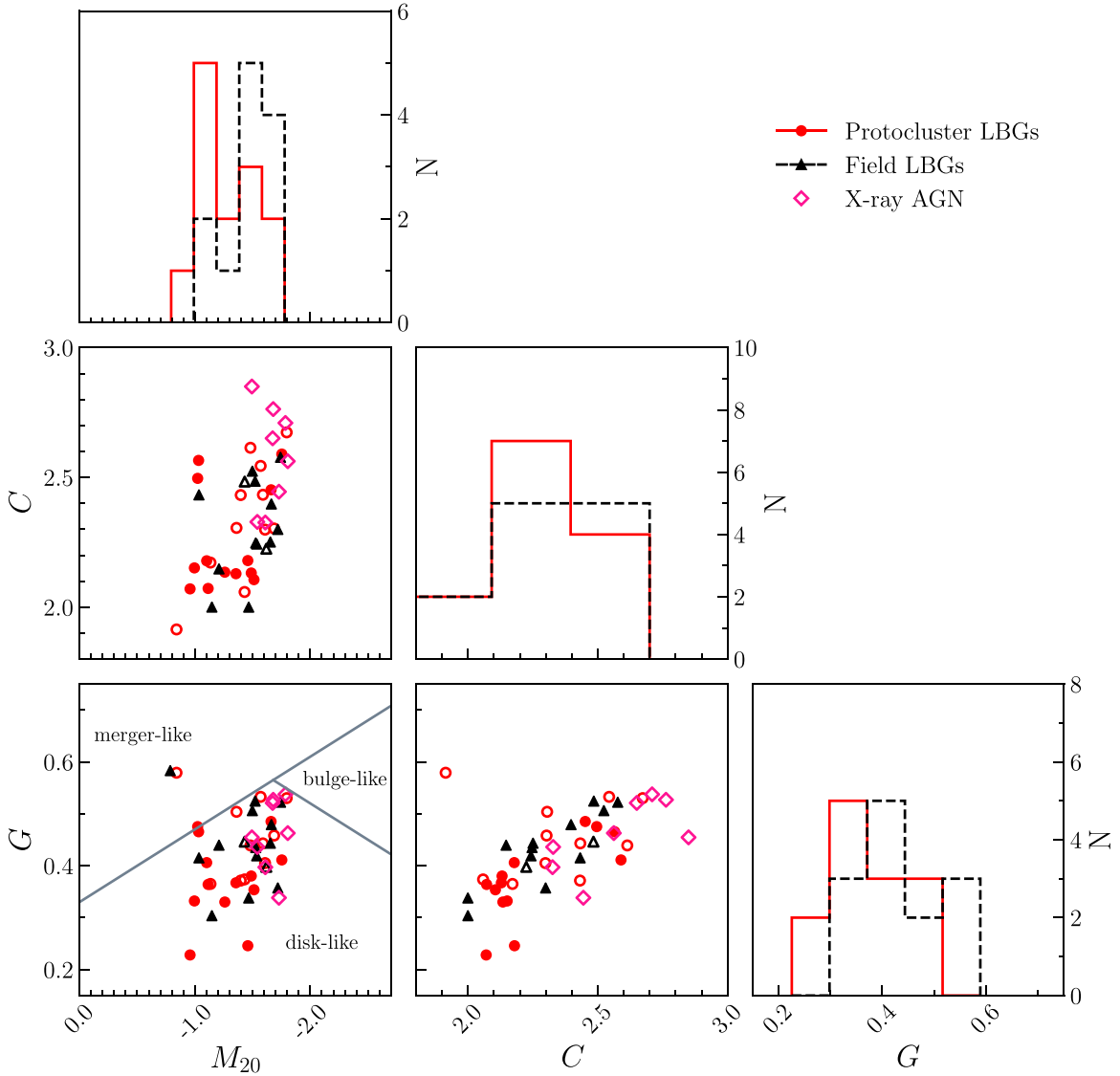


Figure 6. We plot the projections in G - M_{20} - C space of the 13 **S03** protocol cluster LBGs (filled circles), 11 **M17** (open circles) protocol cluster LBGs, 13 **S03** field LBGs (filled triangles), 2 **M17** field LBG (open triangles), and 8 X-ray detected protocol cluster AGN (open diamonds), where G is the Gini coefficient, M_{20} is the second-order moment of light, and C is the concentration statistic. For reference, we also plot the G - M_{20} classification regions of Lotz et al. (2008). While we show both **S03** and **M17** LBGs in the scatter plots, we restrict the histograms to the **S03** LBG sample.

the **S03** LBGs alone suggest that the the protocol cluster LBGs are flatter than their field counterparts: the test for G admits the rejection of the null hypothesis, and the tests on the G - M_{20} and G - C joint distributions also suggest differences in the distributions of light of protocol cluster and field galaxies. However, the protocol cluster and field galaxies do not cleanly separate in any of the projections of G - M_{20} - C space. Additionally, if we include the **M17** LBGs, all of the KS tests on the nonparametric morphological measures are consistent with the null hypothesis. Thus, we are unable to draw any conclusions about morphological differences between the protocol cluster and field LBGs.

3.4. Visual Classification

For a direct comparison of our rest-frame optical morphologies with Hine et al. (2015), we also pursued a similar visual classification scheme for protocol cluster candidate LBGs using F160W images. Cutouts of SSA22 LBGs were mixed with

cutouts of LBGs from the GOODS-N field and blindly distributed to seven voters, who placed each galaxy in one of six categories, as defined in Hine et al. (2015):

1. C1: One clearly distinct, compact nucleus.
2. C2: Single nucleus, but less compact or with minor asymmetry.
3. M1: Clear evidence of a second nucleus; all flux falls in a $1''$ diameter aperture centered at the source position.
4. M2: Clear evidence of a second nucleus; some flux falls outside the $1''$ aperture.
5. M3: More than two nuclei or more complex clumpy structure; some flux falls outside the $1''$ aperture.
6. M4: More than two nuclei or more complex clumpy structure; all flux falls inside the $1''$ aperture.

Voters were asked to assign a confidence level from 1 (low) to 5 (high) to their classification, which we use to weight the votes. To artificially enforce consensus on our classifications, we summed the confidence scores of the voters for each galaxy

Table 5
Number of Galaxies in Each Category and Calculated Merger Fraction for Each of Our Visual Classification Samples

| Sample | Number in Category | | | | | | Mergers | Isolated | Merger Fraction |
|---------------|--------------------|----|----|----|----|----|---------|----------|------------------------|
| | M1 | M2 | M3 | M4 | C1 | C2 | | | |
| Protocluster | 0 | 2 | 1 | 0 | 1 | 4 | 3 | 5 | $0.38^{+0.37}_{-0.20}$ |
| X-ray AGN | 1 | 2 | 0 | 0 | 2 | 1 | 3 | 3 | $0.50^{+0.49}_{-0.27}$ |
| Total Field | 9 | 6 | 4 | 1 | 17 | 12 | 20 | 29 | $0.41^{+0.11}_{-0.09}$ |
| GOODS-N Field | 8 | 6 | 4 | 1 | 11 | 8 | 19 | 19 | $0.50^{+0.14}_{-0.11}$ |
| SSA22 Field | 1 | 0 | 0 | 0 | 6 | 4 | 1 | 10 | $0.09^{+0.21}_{-0.08}$ |

Notes. The categories M 1–4 and C 1–2 are defined in Section 3.4. The uncertainty on the merger fraction is calculated using Poisson statistics.

and set a confidence threshold of 65%, classifying galaxies with $\geq 65\%$ of the total confidence in categories M1, M2, M3, and M4 as mergers, while galaxies with a $\geq 65\%$ of the total confidence in categories C1 and C2 were classified as isolated. This threshold was chosen to exclude cases where voters were split 4-to-3 between merger and isolated categories. This method excludes two protocluster LBGs and one X-ray AGN for which the confidence threshold is not met (i.e., the voters were not confident in classifying the galaxy as a merger or isolated). We classify these galaxies as “ambiguous.” A plurality of votes for these ambiguous galaxies place them in category C2, which allows for diffuse morphology and asymmetry about a single nucleus. This is consistent with the voting scheme in Hine et al. (2015), where many ambiguous galaxies were classified as C2. We also used the confidence scores to assign each galaxy a final category from the above list by weighting each vote by the voter’s assigned confidence. We show the results of this analysis in Table 5 and Figure 7.

The outcome of our visual classification of LBGs supports the results of the parametric and nonparametric morphological analyses, finding no significant difference in the observed fraction of galaxies in mergers between the SSA22 protocluster and the combined $z \sim 3$ field. Specifically, we find merger fractions of $0.38^{+0.37}_{-0.20}$ for protocluster LBGs, $0.50^{+0.49}_{-0.27}$ for the X-ray selected protocluster AGN, and $0.41^{+0.11}_{-0.09}$ for the combined SSA22 and GOODS-N field samples. We note also that, if we consider the case where all of the ambiguous cases mentioned above were, in reality, mergers, we would have a protocluster LBG merger fraction of $0.50^{+0.34}_{-0.22}$, which remains consistent with the GOODS-N and combined field merger fractions. However, our reported merger fraction of $0.09^{+0.21}_{-0.08}$ for the SSA22 field is based on one identified merger and is considerably lower than the merger fraction of $0.50^{+0.14}_{-0.11}$ for the GOODS-N field. Additionally, Hine et al. (2015) report a merger fraction of 0.33 ± 0.18 for the SSA22 field based on F814W ACS imaging data. We note that we use a different redshift range to define $z \sim 3$ field galaxies: Hine et al. (2015) used galaxies from $2.5 \leq z \leq 3.5$ in their field samples, while we include only galaxies with $2.9 \leq z \leq 3.3$. However, this does not appear to be a significant driver of the very low merger fraction we observe in the SSA22 field: if we widen our criteria to include galaxies with $2.5 \leq z \leq 3.5$, the field merger fractions remain consistent with the values reported above.

Regardless of the redshift range we adopt, if we assume that the true merger fraction in the SSA22 field is equal to the GOODS-N merger fraction, we find a Poisson probability of $p < 0.03$ that we would observe one or fewer mergers among the SSA22 field LBGs classified here by chance alone. If we compare the SSA22 protocluster and field directly by assuming

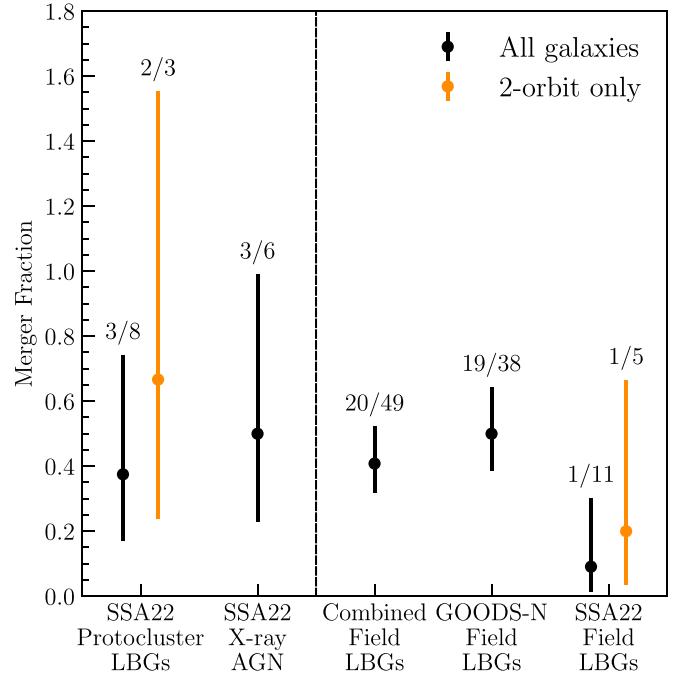


Figure 7. We show the fraction of **S03** LBGs in classes M1 – 4 for the protocluster, combined field, GOODS-N field, and SSA22 field, along with the fraction of X-ray selected protocluster AGN in merger classes. In orange, we show the merger fractions for the protocluster and SSA22 field if we consider only galaxies in two-orbit images. The uncertainty on the merger fraction is derived from Poisson statistics. The vertical dashed line separates protocluster and field merger fractions.

that the protocluster merger fraction is correct, we find that the elevation seen in Table 5 and Figure 7 is apparently marginal: there is a Poisson probability $p < 0.09$ of observing a merger fraction less than or equal to the SSA22 field merger fraction, regardless of how we define the field.

Varying WFC3 IR imaging depth across the SSA22 field of view appears to play a role in the classification of galaxies as merging or isolated, and may be the primary driver of the protocluster-over-field elevation of the merger fraction that we observe in SSA22. If we divide the galaxies by depth, we find two-orbit merger fractions $0.67^{+0.89}_{-0.43}$ (2/3) for protocluster LBGs and $0.20^{+0.73}_{-0.06}$ (1/5) for SSA22 field LBGs, and one-orbit merger fractions $0.20^{+0.73}_{-0.06}$ (1/5) and $0.00^{+0.31}_{-0.00}$ (0/6) for the protocluster and SSA22 field LBGs, respectively. Again assuming that the merger fraction calculated from the GOODS-N LBG sample represents the true field galaxy merger fraction at $z \sim 3$, we calculate the Poisson probability of finding a merger fraction less than or equal to the observed SSA22 field

merger fraction in the two-orbit (one-orbit) images to be 0.29 (0.05). If we evaluate the significance of the protocluster-over-field elevation after separating the galaxies by depth, we find that the elevation is no longer significant: if we assume the merger fraction from the two-orbit (one-orbit) protocluster galaxies, we find a Poisson probability of 0.16 (0.30) of observing a merger fraction less than or equal to the SSA22 field merger fraction at the same depth.

We take this to mean that our classification misses some mergers at single-orbit depth, consequently underestimating the SSA22 field merger fraction, since the sample of SSA22 field galaxies we classified coincidentally contains a larger proportion of galaxies observed at single-orbit depth. Our merger classifications require that the irregular morphological features induced by a merger be discernible by eye; it is possible that the lower S/N in the single-orbit images obscures the low surface brightness features associated with the late stages of a merger. Given these issues, the small number of sources in our samples, and the small number of sources observed at two-orbit depth, our constraints on any enhancements on merger fractions in the protocluster compared to the field are weak and not statistically significant at present.

The wavelength range of our observations is also expected to affect how many galaxies are classified as mergers. Hine et al. (2015) used rest-frame UV ACS F814W observations to classify their galaxies. Over their adopted redshift ranges, this probes wavelengths (based on the F814W reference wavelength) $\sim 1960\text{--}1990\text{ \AA}$ in the protocluster and $\sim 1790\text{--}2310\text{ \AA}$ throughout the range $2.5 \leq z \leq 3.5$. High angular resolution and the ability to trace star formation have made rest-frame UV observations a typical choice for merger classification (e.g., Lotz et al. 2004, 2006), though we note that the patchiness of UV observations due to individual star-forming clumps may make otherwise “ordinary” star-forming galaxies look irregular. In our case, our F160W observations probe (again based on the filter reference wavelength) $\sim 3740\text{--}3790\text{ \AA}$ in the protocluster and $\sim 3580\text{--}3950\text{ \AA}$ throughout the range $2.9 \leq z \leq 3.3$. Over this range of redshift, the 4000 \AA break moves through the F160W bandpass. By construction and because of the cosmological constraints of observing at $z \sim 3$, the galaxies in our LBG sample are dominated by young stellar populations and consequently have weak 4000 \AA breaks (see, e.g., the model SEDs in Figure 9). Since there is significant continuum emission on either side of the break in our galaxies, we do not expect that observing across the 4000 \AA break should impact our morphological classifications in any significant way.

4. SED Fitting and Physical Property Analysis

To quantify the stellar mass distribution of our sample, we fit the SEDs of LBGs in the redshift range $2.9 \leq z \leq 3.3$. To avoid biasing our measurements of stellar masses and star formation rates, we exclude galaxies known from the literature to be hosting AGN and galaxies with rest-frame $8\text{--}32\text{ keV}$ luminosities $\geq 10^{43.5}\text{ erg s}^{-1}$ (Lehmer et al. 2009a). We require the SSA22 galaxies we fit to have optical-to-NIR photometry available from Kubo et al. (2013), and we extract F160W fluxes from our own images. For consistency with the Kubo et al. (2013) photometry, we deconvolve our F160W images from the PSF described in Section 2.1, smooth the result to a Gaussian PSF with a $1''$ FWHM, and extract photometry from a $2''$ diameter circular aperture. We use all of the filters listed in

Table 6
SED Fitting Filters for Each Sample

| Sample | Observatory/Instrument | Filter(s) |
|----------------------|------------------------|--|
| SSA22 ^a | SUBARU/ SUPRIMECAM | $u^* B V R i' z'$ |
| ... | SUBARU/MOIRCS | $J K_s$ |
| ... | HST/WFC3 | F160W |
| ... | Spitzer/IRAC | $3.6\text{ }\mu\text{m } 4.5\text{ }\mu\text{m } 5.8\text{ }\mu\text{m } 8.0\text{ }\mu\text{m}$ |
| GOODS-N ^b | KPNO/4 m/MOSAIC | U |
| ... | LBT/LBC | U |
| ... | HST/ACS/WFC | F435W F606W F775W F814W F850LP |
| ... | HST/WFC3 | F105W F125W F140W F160W |
| ... | CFHT/WIRCam | K_s |
| ... | SUBARU/MOIRCS | K_s |
| ... | Spitzer/IRAC | $3.6\text{ }\mu\text{m } 4.5\text{ }\mu\text{m } 5.8\text{ }\mu\text{m } 8.0\text{ }\mu\text{m}$ |
| ... | Spitzer/MIPS | $24\text{ }\mu\text{m } 70\text{ }\mu\text{m}$ |

Notes.

^a With the exception of F160W, the SSA22 photometry was measured by Kubo et al. (2013). F160W photometry was extracted from our images using the same procedures as Kubo et al. (2013).

^b See Barro et al. (2019) for description of the procedures used to extract the GOODS-N photometry.

the top half of Table 6, where available. Some of our SSA22 galaxies are not detected in the u^* band due to their strong Lyman breaks, and some galaxies do not have photometry available in all four IRAC bands. We exclude missing and nondetected bands from the fits.

For the GOODS-N sample, we used the photometric uncertainties derived by Doore et al. (2021). These uncertainties were recalibrated to include systematic uncertainties beyond single-instrument calibration, including the use of different photometric methods and systems in the observations, uncertainty and variation in Galactic extinction, blending of sources, and systematic effects created by the assumptions of our SED model.

We performed SED fitting using *Lightning* (Eufrasio et al. 2017), which fits nonparametric star formation histories (SFHs) in discrete, variable, or fixed-width stellar age bins. We made use of the most recent update to *Lightning*, which uses an adaptive Markov chain Monte Carlo (MCMC) algorithm (Doore et al. 2021). We chose SFH bins of 0–10 Myr, 10–100 Myr, 100 Myr–1 Gyr, and 1–2 Gyr, where the upper age limit of the final bin is allowed to vary based on the age of the universe at the redshift of the galaxy being fit. We assumed a Kroupa IMF (Kroupa 2001) and fit using two metallicities, Z_\odot and $0.655Z_\odot$, corresponding to the average metallicity of the universe at $z = 3.1$ as given by the best-fit model in Madau & Fragos (2017). To generate the stellar population models, we used PÉGASE (Fioc & Rocca-Volmerange 1997, 1999), running it once for each metallicity. For intrinsic attenuation, we adopted a Calzetti et al. (2000) extinction law, modified as in Noll et al. (2009) to include a UV bump at 2175 \AA and a parameter δ to control the slope of the attenuation curve. We further modified the attenuation curve by including a birth cloud component, which is applied to the emission from the stars in only the youngest age bin. Our SED model then has a total of seven free parameters: four SFH coefficients and three attenuation parameters. For a more

thorough description of the stellar emission and attenuation prescriptions available in `Lightning`, we refer the reader to Eufrasio et al. (2017) and Doore et al. (2021). To account for Galactic reddening, we used the standard Fitzpatrick (1999) curve. The Galactic A_V varies with the position of each galaxy, based on the Galactic dust extinction estimates of Schlafly & Finkbeiner (2011), which we retrieved using the IRSA DUST web application.¹⁴

We find the quality of our fits to both SSA22 LBGs and GOODS-N LBGs acceptable based on the distributions of χ^2 for each sample. For the fits with $Z = 0.655Z_\odot$, the median and 16th to 84th percentile range of the χ^2_{\min} distribution is $5.79^{+3.69}_{-2.98}$ for the SSA22 LBGs we discuss below, with a median of 6 degrees of freedom, and $11.03^{+9.45}_{-4.58}$ for the GOODS-N LBGs, from a median of 10 degrees of freedom (note that the number of degrees of freedom is larger for the GOODS-N galaxies due to the larger number of available bands; see Table 6). This corresponds to probabilities $p_{\text{null}} = 0.40^{+0.39}_{-0.29}$ for the SSA22 LBGs and $p_{\text{null}} = 0.24^{+0.47}_{-0.20}$ for the GOODS-N LBGs; here, we define p_{null} as the probability of accepting the hypothesis that the data are generated by the model. The majority of fits are thus not ruled out by a χ^2 test. The quality of the fits does not change significantly for the fits with $Z = Z_\odot$.

We show example SED and SFH fit results in Appendix B. The SFH parameters are sampled from the last 1000 steps of the MCMC chains. We use the sampled SFH to calculate the stellar mass of each galaxy, and compute the recent star formation rate (SFR) over the last 100 Myr as the age-bin-weighted average of the most recent two bins of the SFH. The mass-weighted age is computed by weighting the average age of the stars in each bin by the mass in the bin.

We show the distributions of stellar mass, SFR, and specific star formation rate (sSFR) in Figure 8. The SSA22 protocluster LBGs largely appear to follow the same star-forming main sequence as the field LBGs, though they populate the upper end. The typical star formation rates of our protocluster LBGs, $20\text{--}200 M_\odot \text{ yr}^{-1}$, are significantly smaller than the IR-derived SFRs for the DSFGs in the core region of the protocluster, which typically range from $\sim 10^2$ to $10^3 M_\odot \text{ yr}^{-1}$ (Umehata et al. 2015; Kato et al. 2016); that is, we are not probing the most intensely star-forming population of the protocluster. Three of the eight galaxies hosting X-ray detected AGN, which we excluded from our SED fitting, have ALMA derived SFR $\approx 220\text{--}410 M_\odot \text{ yr}^{-1}$, and the remaining five, which are not ALMA-detected, have upper limits $< 130\text{--}210 M_\odot \text{ yr}^{-1}$. These upper limits are consistent with the LBGs in our sample with the largest SFRs.

Two-sample KS tests comparing the SFH-derived properties of S03 protocluster and field LBGs (see Table 4) indicate a significant difference between the protocluster and field distributions of stellar mass; in Figure 8, the protocluster galaxies cluster at higher masses than field galaxies. One of the M17 LBGs, J221718.04+001735.5, is best fit by an extremely high SFR on the order of $10^3 M_\odot \text{ yr}^{-1}$. Visual inspection of this galaxy (see Figure 4) shows that there is a bright unrelated point source nearby, which may be blended with the galaxy in near-IR photometry, producing an IR-heavy, high-attenuation, high-SFR best-fit SED with $p_{\text{null}} = 0.99$. We therefore exclude it when we perform KS tests on the combined S03 and M17 LBG samples. The KS tests on the

combined LBG samples indicate significant differences between the protocluster and field distributions of stellar mass and SFR, with protocluster galaxies having, on average, larger masses and larger SFR. There does not appear to be a significant difference between the sSFR distributions of the protocluster and field galaxies (as visible in Figure 8) or the mass-weighted age distributions of the protocluster and field galaxies.

We took advantage of our nonparametric SFH fitting technique to investigate the average SFH of SSA22 protocluster LBGs. The SFR ψ_i in each of our four stellar age bins is fit as a free parameter. We constructed a sample average SFH chain for the protocluster and field samples by averaging the ψ_i values across each sample's chains. For this exercise, we used the last 1000 values of ψ_i in the MCMC chains, thus yielding sample average SFH chains with 1000 entries. We then sampled the sample average SFH chains to construct the average SFH and model SED of both samples, which we show in Figure 9. Regardless of the assumed metallicity, we find that the SFH of the protocluster sample is significantly elevated over the combined field SFH; for the fits with subsolar metallicity, we find that the SFH is more significantly elevated at the earlier times, while for solar metallicity, we find that the elevation is more significant for the most recent age bin. For an assumed metallicity of $Z = 0.655Z_\odot$ ($Z = Z_\odot$), the maximum SFR enhancement for S03 protocluster LBGs is $2.36^{+0.46}_{-0.63}$ ($2.02^{+0.82}_{-0.70}$)¹⁵ in the 10–100 Gyr (0–10 Myr) stellar age bin. We list the protocluster-over-field SFH ratio for both metallicities and each stellar age bin in Table 7.

Due to the elevation of the mean protocluster SFH over the mean field SFH, the mass of the mean protocluster LBG as determined from the mean SFH is greater by a factor of 1.99 than the mean field LBG: the mean S03 protocluster LBG has $\log M_*/M_\odot = 10.31^{+0.07}_{-0.07}$ while the mean S03 field LBG has $\log M_*/M_\odot = 10.01^{+0.02}_{-0.02}$. We find that the mean protocluster LBG has a mass-weighted age consistent with the mean field LBG: $\log t_{\text{AGE}}/\text{yr} = 8.85^{+0.04}_{-0.04}$ for the protocluster LBGs, and $\log t_{\text{AGE}}/\text{yr} = 8.84^{+0.02}_{-0.02}$ for the field LBGs.

If we construct sample average attenuation curves by treating the attenuation parameters in the same way as the SFH, we find that the protocluster LBGs are more attenuated than their field counterparts. For the fits with $Z = 0.0655Z_\odot$, the optical depth in the rest-frame V-band, τ_V , is $0.49^{+0.06}_{-0.07}$ for the mean S03 protocluster LBG and $0.19^{+0.02}_{-0.02}$ for the mean S03 field LBG.

The larger contribution to the SED from the older stellar population and the increased attenuation together produce a mean protocluster LBG SED slightly redder than the mean field LBG SED. We computed IR colors from the model SEDs in Figure 9, finding that protocluster and field LBGs may be distinguished by future observations with JWST bands: $J - F444W = 1.68^{+0.46}_{-0.43}$ for the protocluster model, while $J - F444W = 1.31^{+0.17}_{-0.17}$ for the field model. However, both SED models are still dominated by young stars. Given the uncertainties on the model parameters, these colors remain uncertain, and color differences between protocluster and field LBGs remain speculative. Observations of the protocluster with JWST, which, with NIRC2, could reach F444W S/N ≈ 60 in 1900 s exposures, will vastly improve the constraints of our

¹⁴ <https://irsa.ipac.caltech.edu/applications/DUST/>

¹⁵ SED-fit derived parameters and their uncertainties are reported as the median and 16th to 84th percentile range of the last 1000 steps in the MCMC chain.

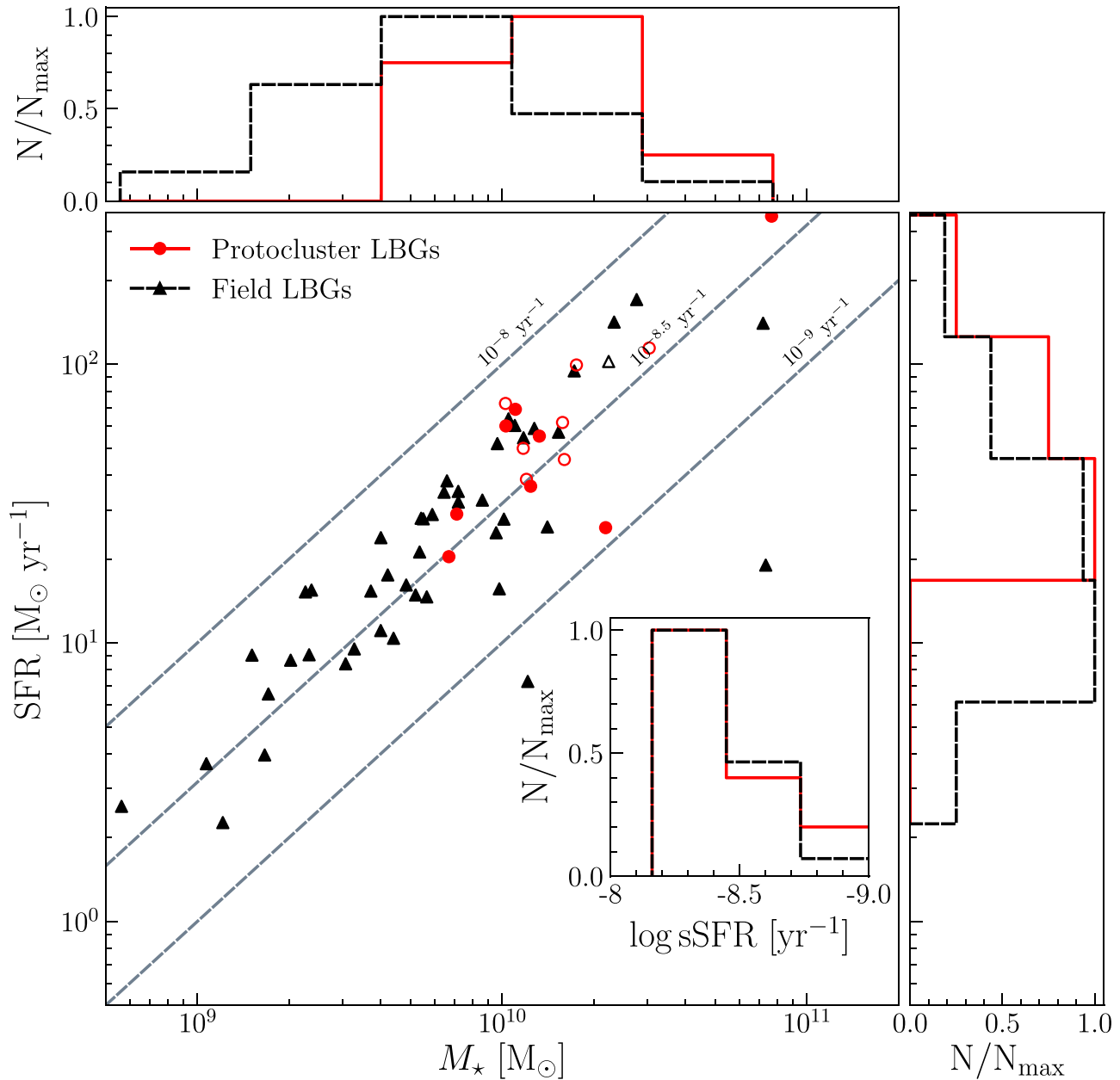


Figure 8. Recent SFR vs. stellar mass M_* for protocluster and field LBGs from the SED fits with $Z = 0.655Z_\odot$. LBGs from the S03 catalog are shown as filled symbols, and LBGs from the M17 catalog as open symbols. For reference, we show dashed lines of constant specific star formation rate (sSFR) in gray, covering 10^{-9} yr^{-1} – 10^{-8} yr^{-1} at increments of 0.5 dex. In the histograms in the margins, we show the distributions of SFR and M_* , and in the inset histogram we show the distribution of sSFR. For the histograms, we again include only LBGs from the S03 catalog. The protocluster LBGs appear to trend toward larger masses and SFR compared to the field LBGs.

SED models across the 4000 \AA break, allowing us to reduce the uncertainties on our models and determine whether the color differences we have extrapolated from the models are real.

5. Discussion

5.1. Star Formation and AGN Enhancement in the SSA22 Protocluster

Lehmer et al. (2009b) suggested two plausible explanations for how the SSA22 protocluster environment might lead to the observed AGN fraction excess: SMBH accretion activity may be increased through (1) more frequent accretion episodes—possibly triggered by major mergers—and higher SMBH accretion rates in the dense regions of the protocluster, or (2)

an increase in the X-ray luminosity of protocluster SMBHs due to the presence of more massive galaxies (and hence SMBHs) in the protocluster.

We have tested scenario 1 by searching for evidence of major mergers in protocluster LBGs detected in the fields of the X-ray detected protocluster AGN. We note that we have not focused directly on the AGN; at the wavelengths we probe, it is difficult to extract morphological information from the AGN, as the AGN contributes significantly to the observed light, resulting in a point-source-like profile superimposed on the host galaxy’s light profile (see, e.g., Figure 6). We have instead focused on the inactive LBG population, to attempt to discern how mergers contribute to the overall growth of galaxies in the protocluster. If major mergers are a significant factor in the

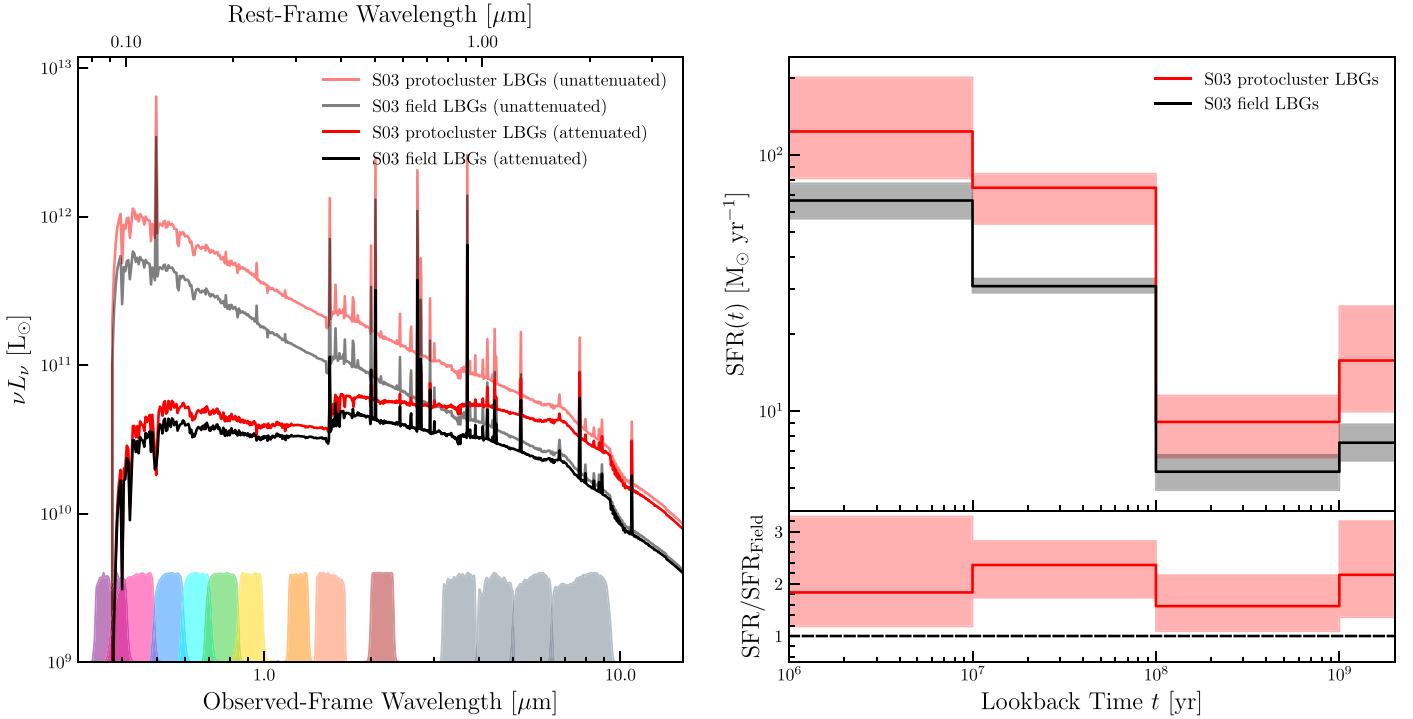


Figure 9. Left panel: we show the sample average model SED for the 8 **S03** protocluster (red) and 45 **S03** field (black) LBGs for which we have SED fits, both before (faded) and after (solid) application of the sample average attenuation model. Underneath the SED, we show the filter curves for the bands we use for fitting for the SSA22 sample (see Table 6), where coverage could be improved throughout the mid-IR to better constrain the attenuation in protocluster galaxies. The protocluster model is more attenuated than the field model. Right panel: we show the sample average SFH of the same protocluster (red) and combined field (black) samples. Below, we show the ratio of the protocluster SFH to the field SFH, with a dashed line at unity for reference. The shaded regions show the 16th to 84th percentile range. In both panels, we show only the results from fitting with $Z = 0.655Z_{\odot}$. For this plot, we have set the redshift for both models at $z = 3.1$.

Table 7

SFR Enhancement as a Function of Time for Both Assumed Metallicities

| Epoch | SFR/SFR _{Field} | |
|------------|--------------------------|------------------------|
| | $Z = 0.655Z_{\odot}$ | $Z = Z_{\odot}$ |
| 0–10 Myr | $1.84^{+1.45}_{-0.65}$ | $2.02^{+0.82}_{-0.70}$ |
| 10–100 Myr | $2.36^{+0.46}_{-0.63}$ | $1.64^{+0.29}_{-0.26}$ |
| 0.1–1 Gyr | $1.57^{+0.59}_{-0.48}$ | $1.73^{+0.60}_{-0.47}$ |
| 1–2 Gyr | $2.17^{+1.03}_{-0.81}$ | $1.91^{+0.56}_{-0.53}$ |

Note. Uncertainties are reported for the 16% to 84% confidence interval.

growth of galaxies in the protocluster, we would expect to observe differences in the morphologies of protocluster and field LBGs. Our results from quantitative and visual morphological analyses suggest that this is not the case: our samples of protocluster and field LBGs appear to be drawn from the same morphological population. We find a marginal result that the protocluster LBGs from the **S03** catalog appear to have larger values of G (indicating flatter distributions of light) than their field counterparts, but when we take other Lyman-break-selected galaxies from the **M17** catalog into account, we find that the Sérsic parameters and nonparametric morphologies of protocluster and field LBGs are consistent with each other. Our results from model fitting suggest that the majority of protocluster LBGs have Sérsic indices $n < 2.5$, consistent with disk-dominated light profiles, even accounting for the effects of noise and the PSF (see Appendix A), which may cause n to be underestimated by up to 50%.

While previous work by Hine et al. (2015) found a marginally elevated merger fraction in the protocluster, we

find that the merger fraction among X-ray AGN in the protocluster is consistent with the merger fractions among **S03** protocluster and field LBGs, though we are limited by the small number of protocluster LBGs we are able to use. We have attempted to go beyond the typical methods for counting mergers by examining the residuals after subtracting Sérsic models for evidence of mergers, finding a merger fraction in rough agreement with the one derived by visual classification, though this is also limited by small numbers.

The increased merger fractions in Hine et al. (2015) may be due to the influence of star formation on their F814W observations, probing the rest-frame UV. Individual UV-luminous clumps of star formation may be difficult to discern by eye from multiple nuclei: in 6 out of 10 cases, the classifications they assigned to protocluster LBGs often indicated “more than two nuclei or complex clumpy structure” rather than clear-cut cases of a double nucleus. In addition, Hine et al. (2015) found that the rest-frame UV asymmetry in protocluster LBGs, often used as a merger diagnostic, indicates fewer mergers than their visual classification; however, at high redshift, calculation of the asymmetry statistic A suffers from the same limitations on resolution and S/N per pixel as we have encountered in computing our own nonparametric morphologies. Comparisons to protocluster merger fractions from the literature outside of SSA22 are limited; Lotz et al. (2013) found a merger fraction of $0.57^{+0.13}_{-0.14}$ in a $z = 1.62$ protocluster (XMM-LSS J02182-05102; also called IRC-0218A). By comparison, they measure a field merger fraction of 0.11 ± 0.03 , indicating significant enhancement of merger activity in the protocluster. The enhancement of merger activity in an overdense environment is also in line with theory: in

studies of Millennium simulation merger trees, Fakhouri & Ma (2009) found that overdensity enhanced merger rate relative to the mean field environment at all redshifts $z \leq 2$. However, their results also suggest that this enhancement grows weaker with increasing redshift, with overdensities at $z \sim 2$ seeing less merger rate enhancement relative to overdensities at lower redshift (see, e.g., Figure 5 in Fakhouri & Ma 2009).

Our discussion thus far has been focused on major mergers (mass ratio ≥ 0.25), which are expected to cause the largest and clearest morphological disturbances and possibly trigger an AGN phase. However, if the overall merger rate is enhanced in overdense environments, minor mergers ($0.10 \leq \text{mass ratio} < 0.25$) should also be more abundant. Our techniques are not particularly well-suited for detection of minor mergers, largely due to surface brightness limits making detection of low-mass satellite galaxies difficult. In particular, the algorithm used to create the $G-M_{20}$ segmentation map tends to exclude low surface brightness satellite galaxies, including only the bright core region of the primary galaxy and thus making the $G-M_{20}$ merger diagnostic insensitive to galaxies accreting lower-mass satellites. In cases where low-mass satellites are segmented properly, their presence still may not move the system in the merger region of the $G-M_{20}$ diagram. Lotz et al. (2010) plotted tracks in $G-M_{20}$ space for the course of mergers at a variety of mass ratios and viewing angles, finding that the $G-M_{20}$ diagnostic is not very sensitive to the early stages of low-mass-ratio mergers. They also find that flyby cases with low mass ratios are not cleanly diagnosed by the $G-M_{20}$ diagnostic and do not trigger long-lasting asymmetries that might be visible by eye. For the visual classifications we performed, the categories we asked the voters to use were designed with major mergers in mind. However, our residual analysis may be more sensitive to minor mergers. Estimating the feature masses and feature mass to total mass ratios of the features we have extracted from the residual images, we found that the masses of some features are consistent with dwarf galaxies, and that the mass ratios approach 0.10 at the low end. Some of the clumpy features we see in the residuals may thus be infalling satellites. While it is possible that low-mass-ratio or early-stage mergers our techniques are less sensitive to could contribute to the enhancement of star formation in the protocluster, studies disagree on whether mergers do (e.g., Zamojski et al. 2011; Kartaltepe et al. 2012) or do not (e.g., Targett et al. 2011) play a significant role in triggering bursts of star formation at $z \sim 2$, suggesting that the influence of mergers on star formation may vary with redshift and among galaxies selected by different methods.

At $z > 1$, the highest-luminosity (bolometric luminosity $\geq 10^{46} \text{ erg s}^{-1}$) AGN are preferentially found in disturbed systems, believed to be evidence of recent mergers, though AGN luminosity and merger fraction both scale with mass at fixed redshift. McAlpine et al. (2020) find, on the basis of EAGLE simulations, that while high-luminosity AGN are more likely to be found in mergers, major mergers are only an effective driver of AGN fraction enhancement for lower-mass ($< 10^{11} M_{\odot}$) host galaxies. Five of the eight protocluster X-ray AGN in our F160W images (those without broad optical emission lines) have stellar mass estimates from optical SED fitting by Kubo et al. (2015a), finding stellar masses in the range $0.3\text{--}2 \times 10^{11} M_{\odot}$, on the edge of where major mergers are expected to be effective triggers for AGN activity from EAGLE simulations.

We note, however, that our reliance on a Lyman-break-selected sample excludes some high-mass galaxies, which are more likely to be found in mergers. Indeed, Kubo et al. (2017) found some evidence of merger-driven evolution in a group of massive quiescent galaxies at the protocluster core. It may then be that, while our results suggest only that the protocluster LBG population (or equivalently, galaxies in an LBG phase of their evolution) are not any more likely to be found in major mergers than their field counterparts and that the protocluster overall may not be a more merger-rich environment than the field, mergers may still play a role in the evolution of the most massive protocluster galaxies.

While our results suggest that accretion due to major mergers is likely not a major environmental difference between the protocluster and field, and hence not the primary source of the X-ray enhancement in the fields we have studied here, galaxy-scale accretion is not ruled out. Recent simulations (e.g., Romano-Díaz et al. 2014) taken together with IFU observations also suggest that major mergers may not be the dominant mode for the accumulation of stellar mass in the SSA22 protocluster. Rather, smooth accretion of gas flows along filaments of the cosmic web between galaxies may power *in situ* star formation, SMBH growth, and AGN activity. These filaments have been imaged in emission in the SSA22 protocluster, and rough calculations estimate that they may contain $\sim 10^{12} M_{\odot}$ of gas available for accretion (Umehata et al. 2019). However, it is difficult to establish whether inflows along these filaments exist, or whether they could carry enough gas into a galaxy to power an AGN.

The nodes of the imaged web notably coincide with the massive, star-forming submillimeter galaxies observed in Umehata et al. (2018). Four out of the eight X-ray AGN studied in Alexander et al. (2016) are colocated with large Ly α nebulae. We find that two of the S03 protocluster LBGs in our GALFITM sample, SSA22a-C47 and SSA22a-M28, are associated with Ly α nebulae from the Matsuda et al. (2004) Ly α blob survey: LAB 11 and LAB 12, respectively. The Sérsic model parameters and nonparametric morphologies for these galaxies are comparable to those for the other protocluster and field LBGs in our sample, and SSA22a-M28 is classified as isolated but slightly irregular by our visual classification scheme, while SSA22a-C47 was not classified by our voters. However, we find some evidence of a possible tidal bridge between SSA22a-C47 and its projected companion when examining its residual after Sérsic model subtraction (see Figure 4). With such a small sample, we are unable to establish whether the LABs, which appear to be associated with AGN activity, are also associated with major mergers. We attempt to draw more detailed connections between the morphologies and physical properties of our LBG sample and their local, Mpc-scale environment in Section 5.2.

We investigated scenario 2 (which already has significant evidence from prior SED fitting and submm studies, e.g., Kubo et al. 2013; Umehata et al. 2018) by fitting the SEDs and nonparametric SFHs of our samples of protocluster and field LBGs. Typical studies of high-redshift AGN focus on hard X-ray detected AGN with large bolometric luminosities, making studies of the physical causes of AGN fraction enhancement difficult to control for mass. The result of Yang et al. (2018) establishes that, at $z > 2$, AGN fraction does not depend on environment when galaxies with similar stellar masses are compared. Galaxies are expected to be more

massive in protoclusters at intermediate redshifts (with $2 \lesssim z \lesssim 4$) when compared to the field (e.g., Steidel et al. 2005; Hatch et al. 2011; Cooke et al. 2014). Since SMBH mass should scale with stellar mass (e.g., Ding et al. 2020; Ferrarese & Merritt 2000), we should thus expect to have enhanced AGN activity in protoclusters with respect to the field at intermediate redshifts (e.g., Lehmer et al. 2009b, 2013; Digby-North et al. 2010; Vito et al. 2020). Using KS tests, we found that the protocluster and field samples appear to be drawn from the same distributions of sSFR and mass-weighted stellar age, while the protocluster galaxies have stellar mass and SFR distributions significantly weighted toward higher mass and higher SFR. We have also found that the mean SFH of our sample of protocluster LBGs is elevated by a factor of about 2 over the mean field LBG SFH in the earliest stellar age bins, from 10 Myr to approximately 2 Gyr. This elevated star formation rate in the oldest stellar population leads to a mean protocluster LBG about 2.2 times more massive than the mean field LBG. Thus, the observed AGN fraction enhancement in the SSA22 protocluster may largely be an effect of the enhanced mass of the typical protocluster galaxy.

5.2. Correlations between Local Environment and Galaxy Properties

To assess the variance in morphology and star formation properties throughout the protocluster, we use a Gaussian kernel density estimation (KDE) to estimate the LAE surface density, Σ_{LAE} . At the location of each $z \approx 3.1$ LAE from Hayashino et al. (2004), we place a circular 2D Gaussian with an FWHM of $2'$, corresponding to 3.75 comoving Mpc. The resulting distribution is renormalized as a surface number density, and sampled at the positions of our protocluster LBG sample. Hayashino et al. (2004) place the threshold of the “high-density region” of the SSA22 protocluster at an LAE surface density of 0.26 arcmin^{-2} . We find that, due to the construction of our fields, all of our LBGs are in the high-density region, and they all have local $\Sigma_{\text{LAE}} > 0.5 \text{ arcmin}^{-2}$, which is >5 times the average density of the control field in Hayashino et al. (2004).

We plot the morphological and physical properties of our samples of protocluster LBGs in Figures 10 and 11, respectively. To examine whether galaxies move through G – M_{20} space as a function of Σ_{LAE} , we define two additional morphological measures, the merger statistic μ and the bulge statistic β , as the signed perpendicular distance from the lines $G = -0.14M_{20} + 0.33$ and $G = 0.14M_{20} + 0.80$, respectively:

$$\mu = 0.14M_{20} + 0.99G - 0.33 \quad (8)$$

$$\beta = -0.14M_{20} + 0.99G - 0.79. \quad (9)$$

Galaxies with more merger-like morphologies (in the sense of Lotz et al. 2008; see Figure 6) thus have larger values of μ , and galaxies with more bulge-like morphologies have larger values of β .

If we suppose that mergers are more common in the denser regions of the protocluster, we should expect the morphologies of galaxies to have identifiable trends with the projected LAE density. We find no strong correlations between the parametric or nonparametric morphological measurements and Σ_{LAE} . There is an apparent downward trend in G , but a Pearson test shows that it is marginal with $p = 0.09$, and n and C , which also probe the concentration of the galaxies, exhibit no such trend. The only other parameter that shows any marginal

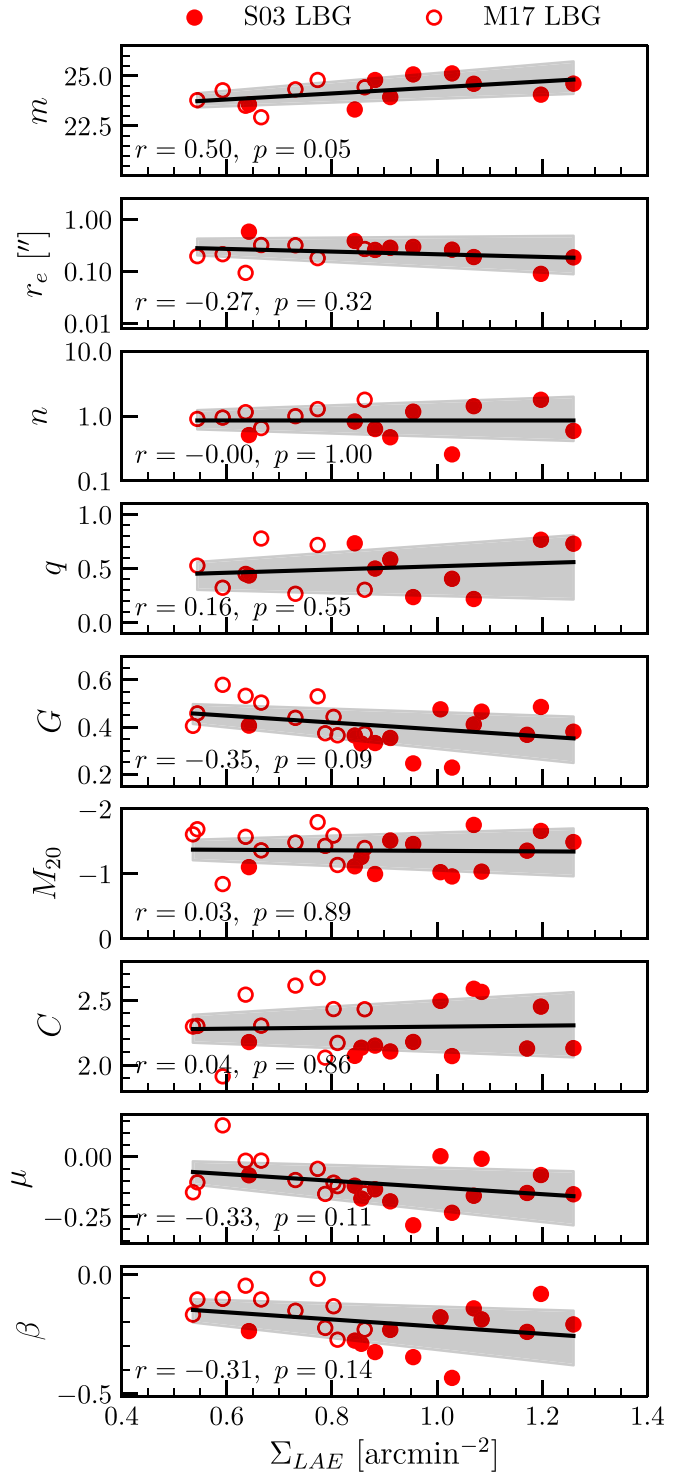


Figure 10. We show all of our morphology measurements as a function of LAE surface density for our sample of protocluster LBGs. From the top panel down: Sérsic model F160W magnitude m , Sérsic fit effective radius r_e , Sérsic index n , Sérsic fit axis ratio q , Gini coefficient G , second-order moment of light M_{20} , concentration index C , and the G – M_{20} merger and bulge statistics μ and β . We show LBGs from the S03 catalog as filled symbols, and LBGs from the M17 catalog as open symbols. For each property, we plot a linear regression to both sets of LBGs with the 16th to 84th percentile interval for the slope (as computed from bootstrap resampling). We print the Pearson test statistic and probability for each measurement when both S03 and M17 LBGs are included in the corner of each panel.

correlation with Σ_{LAE} is the Sérsic model magnitude m ($r = 0.50$, $p = 0.05$), growing fainter with increasing density. We find that this is likely due to biases in our images: the two-

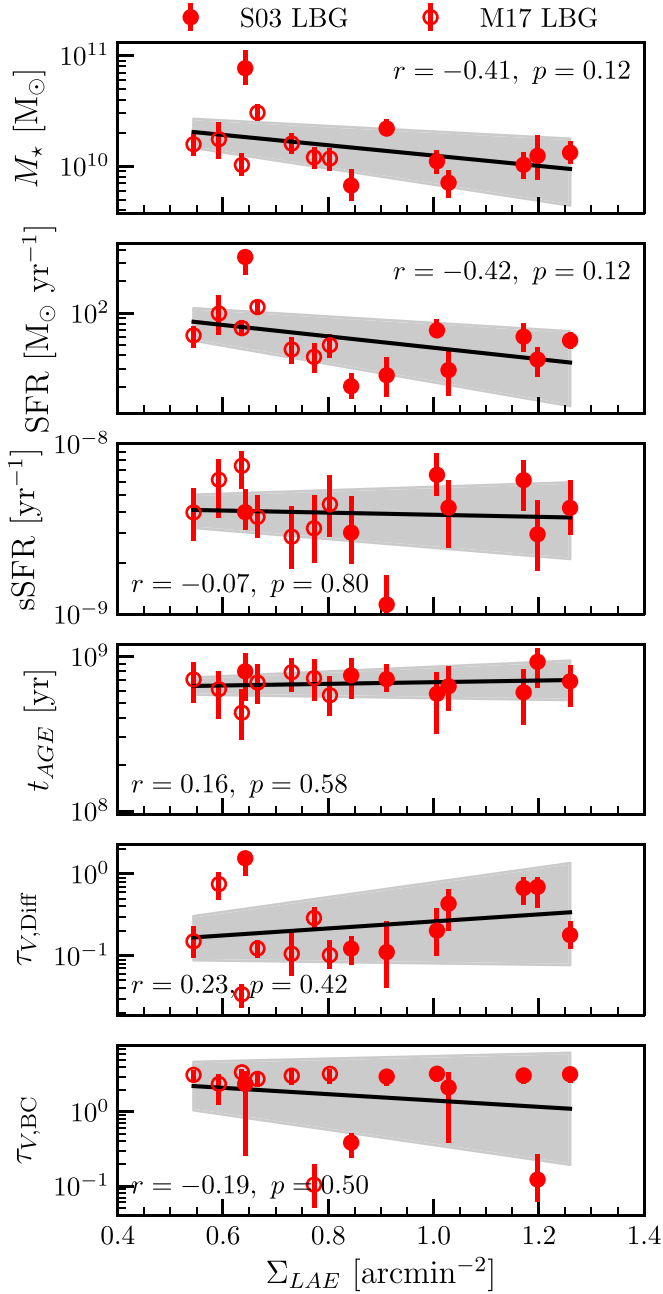


Figure 11. We show all of our SFH-derived measurements as a function of LAE surface density for the $Z = 0.655Z_{\odot}$ SED fits to our sample of protocluster LBGs. From the top panel down: stellar mass M_* , star formation rate over the last 100 Myr, specific star formation rate over the last 100 Myr, mass-weighted age t_{AGE} , diffuse optical depth at the rest-frame V-band $\tau_{\text{V,Diff}}$, and birth cloud optical depth at the rest-frame V-band $\tau_{\text{V,BC}}$. We show LBGs from the S03 catalog as filled symbols, and LBGs from the M17 catalog as open symbols. For each property, we plot a linear regression to both sets of LBGs with the 16th to 84th percentile interval for the slope (as computed from bootstrap resampling). We print the Pearson test statistic and probability for each measurement when both S03 and M17 LBGs are included in the corner of each panel.

orbit depth images we use are targeted on the denser regions, so in the less dense regions we preferentially select brighter galaxies, and only brighter galaxies have acceptable Sérsic fits. If we repeat the Pearson test for all S03 and M17 protocluster LBGs regardless of Sérsic fit quality, using the F160W aperture magnitudes we measured for SED fitting, we find that in this larger sample there is no significant correlation between

magnitude and Σ_{LAE} . Kubo et al. (2013) and Kubo et al. (2017) found that several massive galaxies in the densest regions of the protocluster have compact sizes and $n > 2.5$ Sérsic profiles similar to local early-type galaxies (ETGs). Our results do not reflect this, though we note that the maximum recovered Sérsic index among our LBGs is < 2 and our F160W imaging and SSA22 LBG samples do not cover the entirety of the “core” region of the protocluster targeted by the ALMA deep fields (ADF). In particular, the AzTEC14 group at the protocluster core (Kubo et al. 2015b), where Kubo et al. (2017) found massive galaxies similar to local ETGs, is not covered by our F160W images. In this region, where the proto-brightest cluster galaxy (BCG) is predicted to be evolving, mergers may be a driving factor behind evolution. However, Kubo et al. (2013, 2017) studied only a subset of the massive galaxies in the protocluster, and Kubo et al. (2017) noted a possible deficiency in low-mass galaxies in the AzTEC14 group, implying that a more sensitive mass-complete sampling of the protocluster core may be necessary to establish whether mergers are ongoing or in the past.

We find that none of the SED-fit-derived physical properties are correlated with Σ_{LAE} . It is well-established that there are intensely star-forming galaxies (many of which also host AGN) in the densest regions of the protocluster with IR-derived star formation rates on the order of 10^2 – $10^3 M_{\odot} \text{ yr}^{-1}$ (see, e.g., Umehata et al. 2015; Alexander et al. 2016; Kato et al. 2016). By the placement of our fields and the construction of our SED fitting sample, which excludes known AGN, we have excluded these DSFGs. Submillimeter observations and previous SED fitting have also shown that there are massive galaxies in the most dense region of the protocluster (e.g., Kubo et al. 2013, 2015b). Our results, which find no strong trend between the SFR or mass of protocluster LBGs and Σ_{LAE} , may not conflict with these established results: it may be that the general star-forming galaxy population is not more massive or more intensely star-forming in the denser regions of the protocluster, but rather that some galaxies in the densest regions (i.e., AzTEC14) are exceptionally massive, the possible predecessors of what will become the BCG as the protocluster evolves. In addition to our results that find that the general LBG population of the protocluster does not appear to be rapidly, currently evolving, we thus also find that it appears that LBGs in denser areas of the protocluster are evolving no more rapidly than elsewhere in the protocluster.

5.3. JWST Prospects for SSA22

While the primary limits on this study are imposed by the small numbers of protocluster and field galaxies, morphological studies at $z \sim 3$ are also limited by the sensitivity and resolution of current near-IR telescopes. Our two-orbit-depth F160W images are insufficient to map the full extent of plausible tidal features, and the angular resolution in our images (slightly less than 500 kpc pix^{-1}) is at the limit of what Lotz et al. (2004) recommend for nonparametric morphological measurements. Next-generation space telescopes such as the James Webb Space Telescope (JWST) will present significant improvements in both regards. The search for low surface brightness tidal features will benefit from improved sensitivity, while quantitative morphological measurements like Sérsic model fitting will also benefit from improved angular resolution throughout the rest-frame optical.

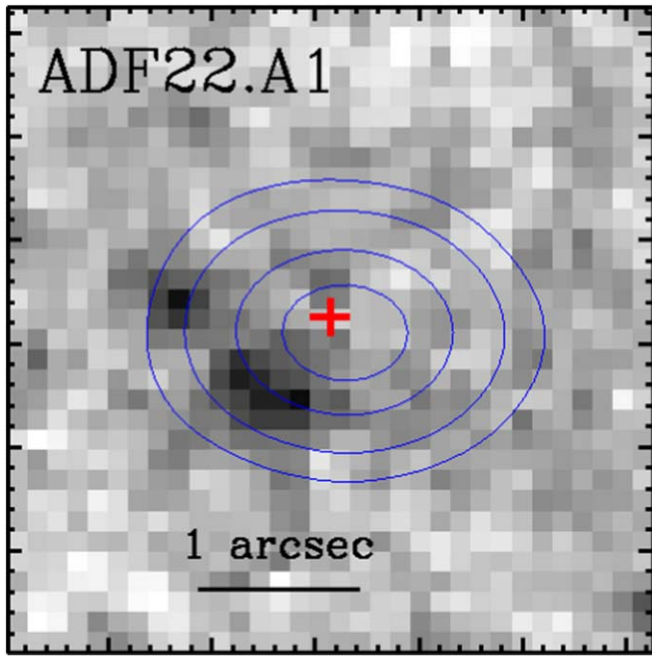


Figure 12. The AzTEC1/ADF22.A1 system, as seen by WFC3/F160W. The system consists of at least two closely associated (<5 kpc) F160W-visible galaxies, with offset Chandra (red cross) and ALMA 1.1 mm (blue contours) detections. The offset source is not detected in ACS bands, and appears very faintly in F160W.

For example, the field of view of our images contains at least one interesting system believed to be a complex merger: the AzTEC1/ADF22.A1 system (Tamura et al. 2010; Umehata et al. 2014, 2015, 2017), shown in Figure 12. The primary component of the system is an ALMA 1.1 detection with a coincident Chandra detection, with faint companion galaxies that are not visible at wavelengths $<1 \mu\text{m}$. The companions, of which there appear to be at least two, are visible in F160W—though they are not included in our catalog, due to the S/N cuts we impose, and they are not Lyman-break-selected, due to their nondetection blueward of $1 \mu\text{m}$. The SED of the system appears to be consistent with an AGN buried in a dusty, highly star-forming galaxy. The system is thus speculated to be a protoquasar, possibly fueled by the major merger of the F160W-detected galaxies nearby. JWST ETC simulations using the currently observed SED suggest that NIRCam and MIRI observations will produce near- and mid-IR detections of all three components of this system at higher resolution than even the currently available HST data, allowing us to search for merger features throughout the IR and to treat this system as a case study in whether mergers fuel AGN in the protocluster environment.

While we have been unable to establish whether major mergers are a dominant mode of growth among galaxies throughout the protocluster, we have not examined the very core of the protocluster where the system that will become the BCG may be evolving. The BCGs in Coma-like clusters, which the SSA22 protocluster is expected to become, are thought to form as the result of successive major mergers in the cluster core. A group of massive galaxies has already been identified in the protocluster core by Kubo et al. (2015b), which may be the site where the future BCG is forming. A larger-than-expected portion of these galaxies are already quiescent and bulge-dominated, suggesting significant evolution and possible

previous merger activity. JWST observations of this system and morphological analyses of its components could allow the detection of merger signatures, giving us a possible window into the early stages of BCG formation.

6. Summary

We have pursued multiple avenues of morphological analysis on protocluster and field galaxies detected in new and archival HST WFC3 F160W images of the SSA22 protocluster. We fit single-Sérsic models to galaxies detected in our images to extract effective sizes and Sérsic indices, and then examined the residual images after model subtraction for evidence of tidal features. We also calculated the Gini coefficient G , moment of light M_{20} , and concentration statistic C for protocluster and field galaxies detected in our images. For a third point of comparison, we used a visual classification scheme modeled on Hine et al. (2015) to examine the observed merger fractions among protocluster and field LBGs.

To supplement our morphological analysis, we fit the UV-to-near-IR SEDs and nonparametric SFHs of a sample of protocluster and field galaxies, in order to measure stellar masses and SFR.

Our main results and conclusions are as follows:

1. Using two-sample KS tests to compare the Sérsic fit morphologies of SSA22 protocluster LBGs to a combined sample of field LBGs from SSA22 and GOODS-N, we find no significant differences in the protocluster and field distributions of any of the model parameters, including effective size r_e ($p_{\text{KS}} \geq 0.37$) and Sérsic index n ($p_{\text{KS}} \geq 0.17$).
2. We find evidence of tidal features in the residual images of both SSA22 protocluster and field LBGs after subtracting the best-fit Sérsic model. Based on this analysis, we estimate rough merger fractions of 0.13–0.44 for protocluster LBGs and 0.14–0.28 for field LBGs. We estimate that the largest and brightest of the plausible tidal features have masses $\log_{10} M_*/M_\odot = 9.78$, suggesting that they may be as massive as the Small Magellanic Cloud.
3. Using two-sample KS tests comparing the nonparametric morphologies of SSA22 protocluster and field galaxies, we find no significant differences in the protocluster and field distributions of M_{20} ($p_{\text{KS}} \geq 0.30$) and C ($p_{\text{KS}} \geq 0.30$). We find a marginal difference between the G distributions of protocluster and field S03 LBGs ($p_{\text{KS}} = 0.04$). However, this is not supported by the KS tests on any of the other measures of the galaxies' concentration (i.e., n and C), and is not evident when M17 LBGs are included in the KS test ($p_{\text{KS}} = 0.25$). We note that only one of the galaxies in which we identify a plausible tidal feature is classified as a merger by the Lotz et al. (2008) cuts in the G – M_{20} plane. We thus hesitate to estimate a merger fraction based on nonparametric morphological analysis.
4. By performing visual merger classifications of selected F160W galaxy cutouts for a direct comparison to Hine et al. (2015), we estimate merger fractions $0.38^{+0.37}_{-0.20}$ among S03 protocluster LBGs and $0.41^{+0.11}_{-0.09}$ among S03 field LBGs. We note that visual classifications from our SSA22 images are limited by the number of S03 LBGs in

our images, and that the number of mergers may be undercounted due to limited depth.

5. We find that the SED fits to our small sample of protocluster and field LBGs are consistent with elevated star formation in the protocluster’s oldest stellar population, with the mean protocluster SFH being significantly elevated over the mean field SFH between lookback times 100 Myr–2 Gyr. The mean protocluster LBG is also more massive and more attenuated by a factor of 2 compared to the mean field galaxy. The mean protocluster LBG is thus slightly redder in terms of IR color, with $J - F444W = 1.68^{+0.46}_{-0.43}$, than the mean field LBG, which has $J - F444W = 1.31^{+0.17}_{-0.17}$. However, young stars are still the dominant contributor to the SEDs of both protocluster and field LBGs.
6. Based on our results, we conclude that the observed enhancement in the SSA22 protocluster AGN fraction may be due to the larger average stellar mass (and hence larger average SMBH mass) of galaxies in the protocluster. In addition, the protocluster LBGs we have studied here appear to have formed more stellar mass earlier than their field counterparts.

Our results are limited throughout by the small number statistics of protocluster LBGs; we are only able to identify 24 protocluster LBGs in our F160W images, and requirements on converged Sérsic fits and available photometry mean that in practice we can only use a fraction of them in our analysis. These limits also mean that our analyses are difficult to control for mass; studies of merger fractions in particular are sensitive to mass, as merger fraction increases with stellar mass at fixed redshift. Our focus on Lyman-break-selected galaxies in this work may also exclude more massive galaxies with more evolved SED shapes (Wang et al. 2019), which may be involved in ongoing mergers or have morphologies that indicate past mergers. We are hopeful that the increased sensitivity of JWST will allow the construction of true mass-selected samples, which will allow deeper studies of the connections between stellar mass, AGN fraction, and overdensity.

We gratefully acknowledge support from STScI grant HST-GO-13844.013-A (E.B.M., B.D.L., B.B.). D.M.A. acknowledges support from the Science and Technology Facilities Council (ST/P000541/1; ST/T000244/1). This work has made use of the Rainbow Cosmological Surveys Database, which is operated by the Centro de Astrobiología (CAB/INTA), partnered with the University of California Observatories at Santa Cruz (UCO/Lick, UCSC).

Facilities: HST (WFC3), Subaru, Spitzer.

Software: *astropy* (The Astropy Collaboration 2013, 2018), *AstroDrizzle* (Fruchter et al. 2010), *SExtractor* (Bertin & Arnouts 1996), *GALFITM* (Vika et al. 2013), *GALAPAGOS-2* (Barden et al. 2012), *Lightning* (Eufrasio et al. 2017), *PÉGASE* (Fioc & Rocca-Volmerange 1997, 1999).

Appendix A

Reliability of Morphological Measurements

We assessed the reliability of our model-fitting and nonparametric analyses with a Monte Carlo technique. We created three sets of *GALFITM* Sérsic models with indices $n = \{1.0, 1.5, 4.0\}$. The other parameters of the model were

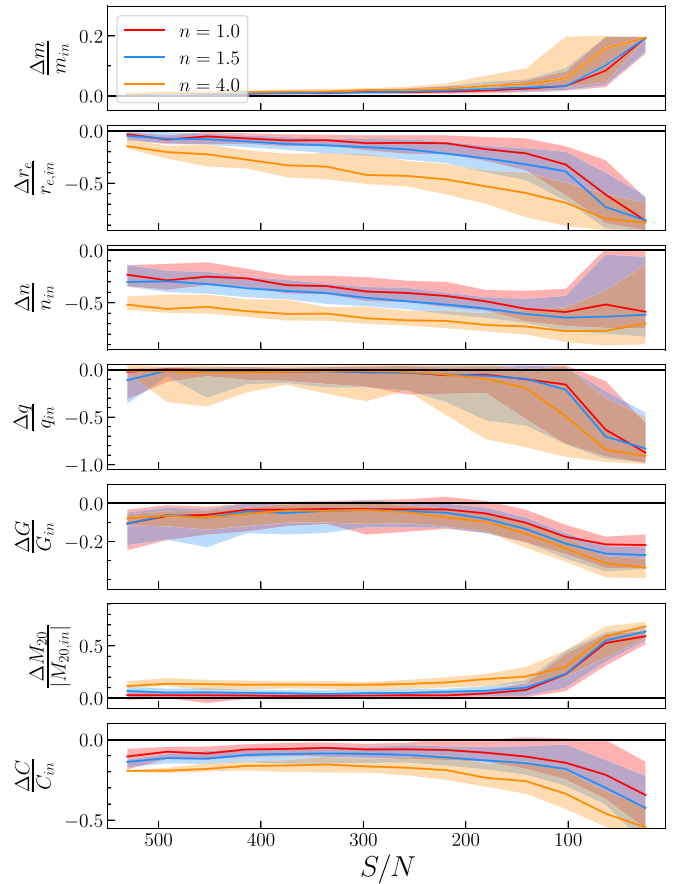


Figure 13. For each morphological measurement, we show the median relative difference between the initial values in three sets of noise-free, unconvolved Sérsic models and the extracted values after PSF convolution and the addition of noise, as a function of the final signal-to-noise ratio in a 1'' diameter aperture. The shaded regions show the 16th to 84th percentile interval.

allowed to vary randomly over their observed ranges. We convolved these synthetic galaxies with our PSF model, added them to blank sky frames from our images, and remeasured their morphologies with *GALFITM* and our nonparametric analysis procedure as described in Section 3.3. We show the relative differences between the recovered morphologies and morphologies as measured from unconvolved, noise-free models in Figure 13.

We find that the reliability of the *GALFITM*-recovered Sérsic radius r_e and axis ratio q are strongly dependent on the S/N, with *GALFITM* consistently underestimating the effective radii of low-S/N galaxies by as much as 75% and consistently converging on unrealistically small axis ratios for low-S/N galaxies. Galaxies with bulge-like $n=4$ profiles are more strongly affected in both cases. There are large errors in the recovered value of the Sérsic index n for all initial values of n and all values of S/N. The recovered value is significantly smaller than the true value in all cases, indicating that the overrepresentation of galaxies with $n \leq 1.0$ in our results may be due to underestimation of the “true” n for these galaxies. However, we note also that the consistent underestimation of n and r_e is expected from the nature of these simulations; convolution with the PSF spreads out the light profile of the model, making it flatter, and the observed effective radius of the model galaxies is naturally decreased by the addition of noise. Since the effects of PSF blurring and Poisson noise cannot be removed from the images in any practical situation,

the “true” values of n and r_e are not necessarily recoverable, and our measurements serve only as a description of the data.

The nonparametric morphological measures are generally more stable with S/N. M_{20} is the most strongly affected, with low-S/N galaxies measured to have significantly larger M_{20} ; that is, the models are observed to be clumpier after convolution with the PSF and the addition of noise.

With the exception of n , r_e , and C (which also depends on measurements of the effective size of the galaxy and is thus biased low even for high S/N), the median relative errors in the morphological measurements are $<10\%$ within the 2σ range for S/N $\gtrsim 100$ and input Sérsic indices 1.0 and 1.5.

As the majority of galaxies in our catalog have Sérsic indices <4 , we take these results to show that our morphological analyses are reliable for our S03 sample (with one exception,

our S03 protocluster LBGs have S/N $\gtrsim 100$, and all of them have $n < 2$). In general, we expect the Sérsic fit results in the catalog to be reliable for the other galaxies in our sample (provided they meet our other criteria for acceptable fits) for S/N $\gtrsim 100$.

Appendix B SED Fit Results

We show the SED fit results with $Z = 0.655Z_\odot$ for our SSA22 LBG samples in Table 8, Figures 14–17. We also show the SED fit results with $Z = 0.655Z_\odot$ for our sample of GOODS-N field LBGs in Table 9 and example fits in Figure 18. For the full set of GOODS-N SED plots, please refer to the online version of this article.

Table 8
SED-fit-derived Physical Properties for Our Samples of SSA22 LBGs

| ID | z^a | $\chi^2_{\min}^b$ | $P_{\text{null}}(\chi^2_{\min})^c$ | M_*^d ($10^9 M_\odot$) | SFR ^e ($M_\odot \text{ yr}^{-1}$) | sSFR ^f (10^9 yr^{-1}) | Age ^g (10^8 yr) | References ^h |
|---------------------|-------|-------------------|------------------------------------|-------------------------------|---|---|---|-------------------------|
| SSA22 Protocluster | | | | | | | | |
| J221721.02+001708.9 | 3.076 | 9.56 | 0.05 | 7.10 | 29.01 | 4.22 | 6.42 | S03 |
| J221718.60+001815.5 | 3.079 | 2.95 | 0.57 | 10.30 | 60.10 | 6.11 | 5.86 | S03 |
| J221727.27+001809.6 | 3.080 | 10.99 | 0.05 | 11.06 | 68.97 | 6.57 | 5.74 | S03 |
| J221731.69+001657.9 | 3.088 | 2.73 | 0.84 | 21.88 | 25.92 | 1.14 | 7.14 | S03 |
| J221718.87+001816.2 | 3.089 | 6.32 | 0.39 | 12.42 | 36.50 | 2.94 | 9.24 | S03 |
| J221737.92+001344.1 | 3.094 | 3.54 | 0.62 | 13.26 | 55.25 | 4.20 | 6.91 | S03 |
| J221719.30+001543.8 | 3.097 | 6.51 | 0.37 | 76.70 | 340.37 | 3.97 | 8.02 | S03 |
| J221720.25+001651.7 | 3.098 | 3.86 | 0.70 | 6.69 | 20.40 | 3.01 | 7.55 | S03 |
| J221732.04+001315.6 | 3.065 | 3.98 | 0.41 | 30.42 | 114.46 | 3.72 | 6.78 | M17 |
| J221701.38+002031.9 | 3.073 | 5.27 | 0.51 | 16.02 | 45.55 | 2.85 | 7.91 | M17 |
| J221718.96+001444.5 | 3.091 | 1.95 | 0.92 | 15.80 | 61.85 | 3.95 | 7.11 | M17 |
| J221718.04+001735.5 | 3.093 | 13.50 | 0.04 | 197.17 | 1707.56 | 9.05 | 2.42 | M17 |
| J221740.98+001127.2 | 3.093 | 4.03 | 0.40 | 17.55 | 99.49 | 6.15 | 6.14 | M17 |
| J221710.35+001920.8 | 3.103 | 7.47 | 0.28 | 10.27 | 72.38 | 7.43 | 4.33 | M17 |
| J221720.55+002046.3 | 3.103 | 2.65 | 0.85 | 11.74 | 49.95 | 4.41 | 5.62 | M17 |
| J221704.34+002255.8 | 3.108 | 11.20 | 0.08 | 12.03 | 38.65 | 3.19 | 7.24 | M17 |
| SSA22 Field | | | | | | | | |
| J221724.44+001714.4 | 3.018 | 6.60 | 0.36 | 12.76 | 58.88 | 4.75 | 5.65 | S03 |
| J221735.98+001708.2 | 3.018 | 7.25 | 0.30 | 10.14 | 27.81 | 2.69 | 5.94 | S03 |
| J221735.30+001723.9 | 3.019 | 2.03 | 0.92 | 8.62 | 32.55 | 3.93 | 6.25 | S03 |
| J221722.90+001608.9 | 3.019 | 9.33 | 0.16 | 12.15 | 7.27 | 0.60 | 8.39 | S03 |
| J221725.64+001612.5 | 3.290 | 8.47 | 0.21 | 15.33 | 57.08 | 3.73 | 8.01 | S03 |
| J221717.69+001900.3 | 3.288 | 4.95 | 0.55 | 22.39 | 102.38 | 4.68 | 5.23 | M17 |

Notes.

^a Redshift from literature; see Section 2.2.

^b Minimum χ^2 of SED fitting chain.

^c Probability of *accepting* the hypothesis that the data were generated by the best-fit model.

^d Stellar mass produced by median SFH.

^e Star formation rate averaged over the last 100 Myr of the median SFH.

^f Specific star formation rate averaged over the last 100 Myr of the median SFH.

^g Mass-weighted age of the median SFH.

^h Catalog reference. S03 = Steidel et al. (2003), M17 = Micheva et al. (2017).

Table 9
SED-fit-derived Physical Properties for Our Sample of GOODS-N field LBGs from the Steidel et al. (2003) Catalog

| ID | z^a | $\chi^2_{\min}^b$ | $P_{\text{null}}(\chi^2_{\min})^c$ | M_*^d ($10^9 M_\odot$) | SFR ^e ($M_\odot \text{ yr}^{-1}$) | sSFR ^f (10^9 yr^{-1}) | Age ^g (10^8 yr) |
|---------------------|-------|-------------------|------------------------------------|-------------------------------|---|---|---|
| J123627.59+621130.1 | 2.917 | 9.52 | 0.48 | 9.66 | 51.92 | 5.45 | 6.29 |
| J123712.30+621138.2 | 2.925 | 4.06 | 0.91 | 2.02 | 8.67 | 4.23 | 7.71 |
| J123706.62+621400.3 | 2.926 | 15.81 | 0.20 | 17.26 | 94.71 | 5.53 | 5.85 |
| J123703.24+621451.3 | 2.926 | 10.06 | 0.26 | 2.26 | 15.24 | 6.84 | 5.17 |
| J123650.40+621055.6 | 2.928 | 12.93 | 0.07 | 0.56 | 2.59 | 4.55 | 6.42 |
| J123644.11+621311.2 | 2.929 | 20.97 | 0.03 | 27.66 | 170.82 | 6.30 | 5.30 |
| J123617.54+621310.1 | 2.930 | 8.78 | 0.27 | 2.33 | 9.06 | 3.81 | 7.72 |
| J123707.72+621038.2 | 2.931 | 13.56 | 0.19 | 5.90 | 28.90 | 4.85 | 6.51 |
| J123647.77+621256.1 | 2.932 | 17.39 | 0.10 | 11.02 | 60.34 | 5.56 | 5.24 |
| J123717.38+621247.4 | 2.939 | 9.71 | 0.47 | 6.60 | 38.16 | 5.83 | 6.55 |
| J123709.34+621047.1 | 2.942 | 9.42 | 0.31 | 1.51 | 9.04 | 5.83 | 5.76 |
| J123647.72+621053.6 | 2.943 | 9.48 | 0.49 | 14.09 | 26.07 | 1.80 | 7.78 |
| J123639.27+621713.4 | 2.944 | 8.62 | 0.57 | 10.50 | 63.71 | 6.17 | 5.57 |
| J123642.40+621448.9 | 2.962 | 6.46 | 0.78 | 2.37 | 15.47 | 6.70 | 4.97 |
| J123646.97+621226.5 | 2.970 | 10.73 | 0.22 | 1.07 | 3.68 | 3.54 | 7.35 |
| J123651.56+621042.2 | 2.975 | 15.80 | 0.15 | 23.33 | 141.81 | 6.14 | 4.69 |
| J123637.15+621547.8 | 2.975 | 5.67 | 0.84 | 5.36 | 21.20 | 4.05 | 5.95 |
| J123635.55+621522.0 | 2.980 | 39.49 | 0.00 | 3.07 | 8.41 | 2.83 | 7.98 |
| J123622.63+621306.4 | 2.981 | 12.44 | 0.26 | 73.39 | 19.02 | 0.26 | 11.20 |
| J123645.04+620940.8 | 2.983 | 13.30 | 0.15 | 4.00 | 11.07 | 2.78 | 9.34 |
| J123647.88+621032.3 | 2.990 | 3.79 | 0.96 | 5.43 | 28.01 | 5.21 | 6.24 |
| J123626.95+621127.4 | 2.993 | 5.99 | 0.74 | 5.51 | 27.89 | 5.06 | 6.28 |
| J123640.93+621358.6 | 3.087 | 10.38 | 0.32 | 9.80 | 15.63 | 1.55 | 9.90 |
| J123650.80+621444.8 | 3.106 | 25.27 | 0.00 | 1.71 | 6.55 | 3.97 | 7.56 |
| J123648.88+621502.6 | 3.115 | 17.99 | 0.08 | 9.57 | 24.85 | 2.53 | 7.21 |
| J123619.40+621502.0 | 3.128 | 8.92 | 0.45 | 4.40 | 10.39 | 2.36 | 8.02 |
| J123658.99+621714.4 | 3.130 | 17.36 | 0.07 | 4.00 | 23.86 | 5.92 | 4.99 |
| J123649.03+621542.4 | 3.136 | 4.24 | 0.94 | 6.45 | 34.75 | 5.41 | 5.09 |
| J123721.63+621350.5 | 3.148 | 31.89 | 0.00 | 3.27 | 9.51 | 3.10 | 8.49 |
| J123645.39+621347.1 | 3.161 | 13.75 | 0.09 | 1.66 | 3.96 | 2.41 | 7.32 |
| J123651.18+621349.0 | 3.163 | 43.97 | 0.00 | 4.85 | 16.13 | 3.43 | 7.52 |
| J123634.88+621253.9 | 3.182 | 26.63 | 0.00 | 1.21 | 2.26 | 1.91 | 8.33 |
| J123653.61+621410.5 | 3.196 | 6.45 | 0.49 | 5.20 | 14.86 | 3.04 | 6.40 |
| J123641.87+621107.4 | 3.197 | 11.33 | 0.33 | 3.71 | 15.34 | 4.09 | 6.22 |
| J123702.70+621426.3 | 3.214 | 17.47 | 0.06 | 71.93 | 140.47 | 1.95 | 8.63 |
| J123641.26+621203.4 | 3.222 | 18.91 | 0.04 | 5.66 | 14.62 | 2.61 | 6.90 |
| J123645.19+621652.4 | 3.229 | 7.35 | 0.60 | 11.77 | 54.49 | 4.64 | 6.17 |
| J123703.26+621635.3 | 3.239 | 46.47 | 0.00 | 7.19 | 34.98 | 4.91 | 5.41 |
| J123637.02+621044.5 | 3.241 | 9.79 | 0.20 | 4.22 | 17.54 | 4.24 | 6.53 |
| J123706.16+621509.9 | 3.246 | 4.84 | 0.77 | 7.19 | 32.01 | 4.40 | 6.55 |

Notes.^a Redshift from Steidel et al. (2003).^b Minimum χ^2 of SED fitting chain.^c Probability of *accepting* the hypothesis that the data were generated by the best-fit model.^d Stellar mass produced by median SFH.^e Star formation rate averaged over the last 100 Myr of the median SFH.^f Specific star formation rate averaged over the last 100 Myr of the median SFH.^g Mass-weighted age of the median SFH.

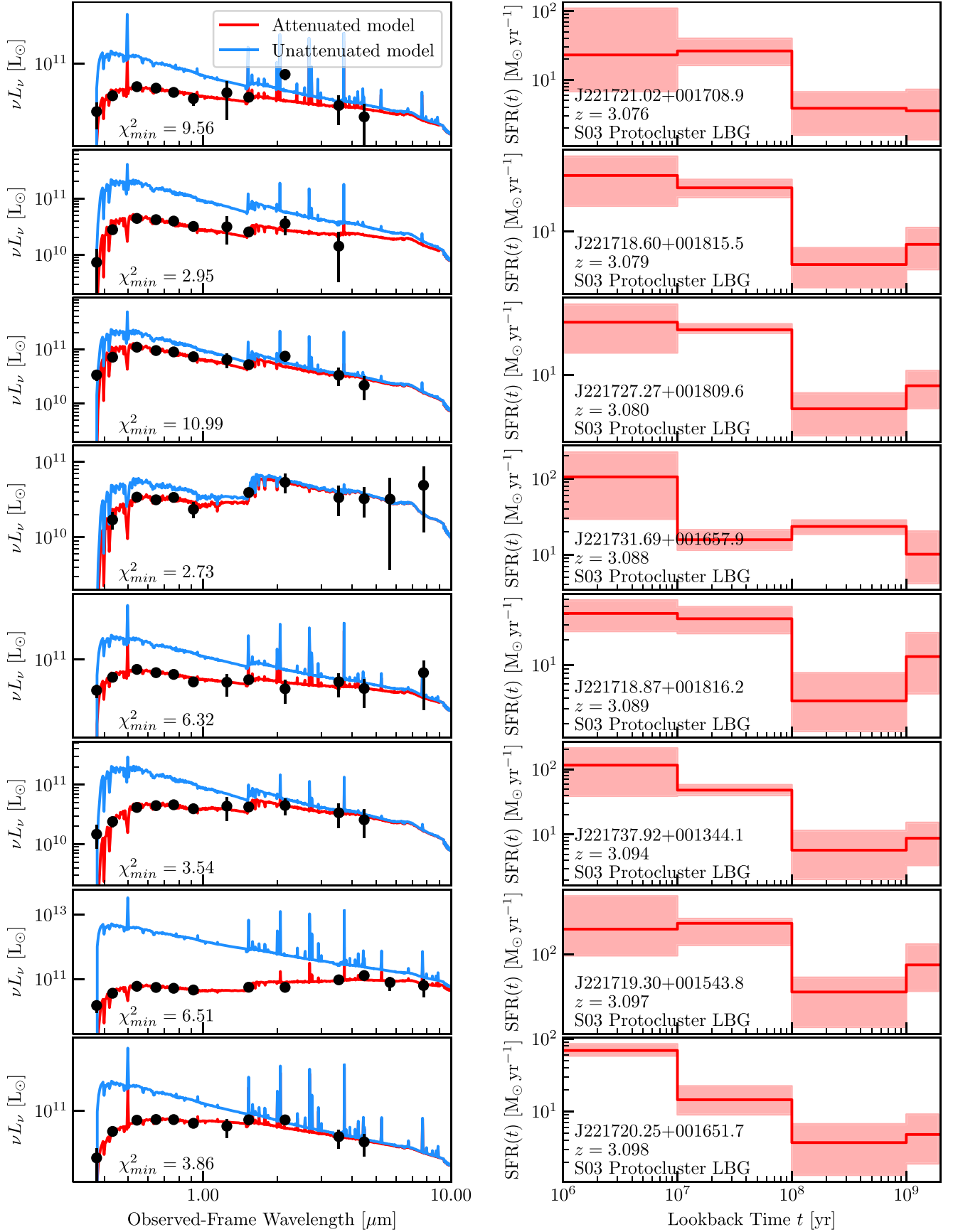


Figure 14. Left: we show the best-fit SED model for each of the eight galaxies in our sample of Steidel et al. (2003) protocluster LBGs that have SED fits. Right: we show the median SFH for the same galaxies. For clarity, we have truncated the last bin of the SFH at 2 Gyr. The shaded regions indicate the 16th to 84th percentile interval.

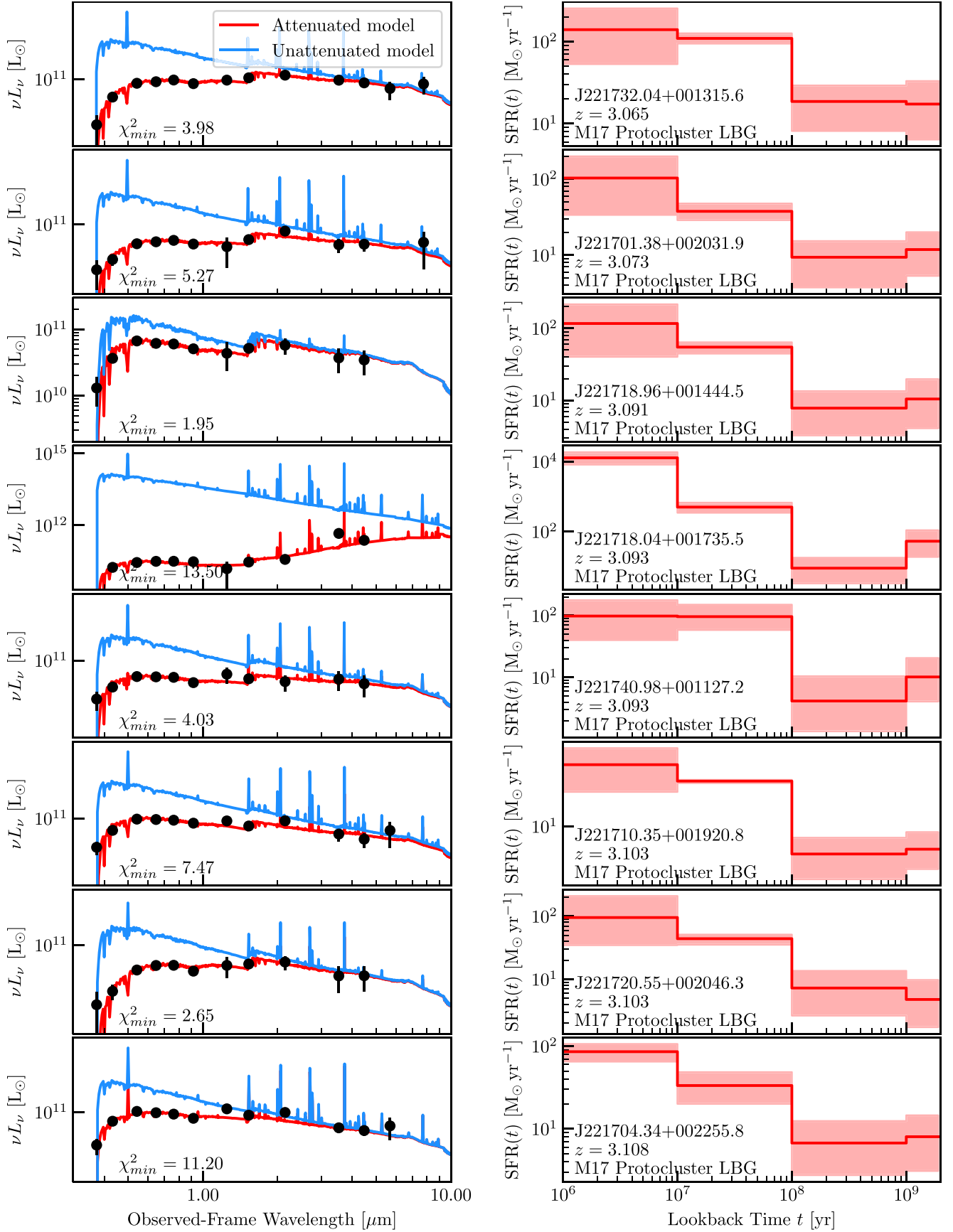


Figure 15. Same as Figure 14, but showing the eight M17 protocluster LBGs with SED fits.

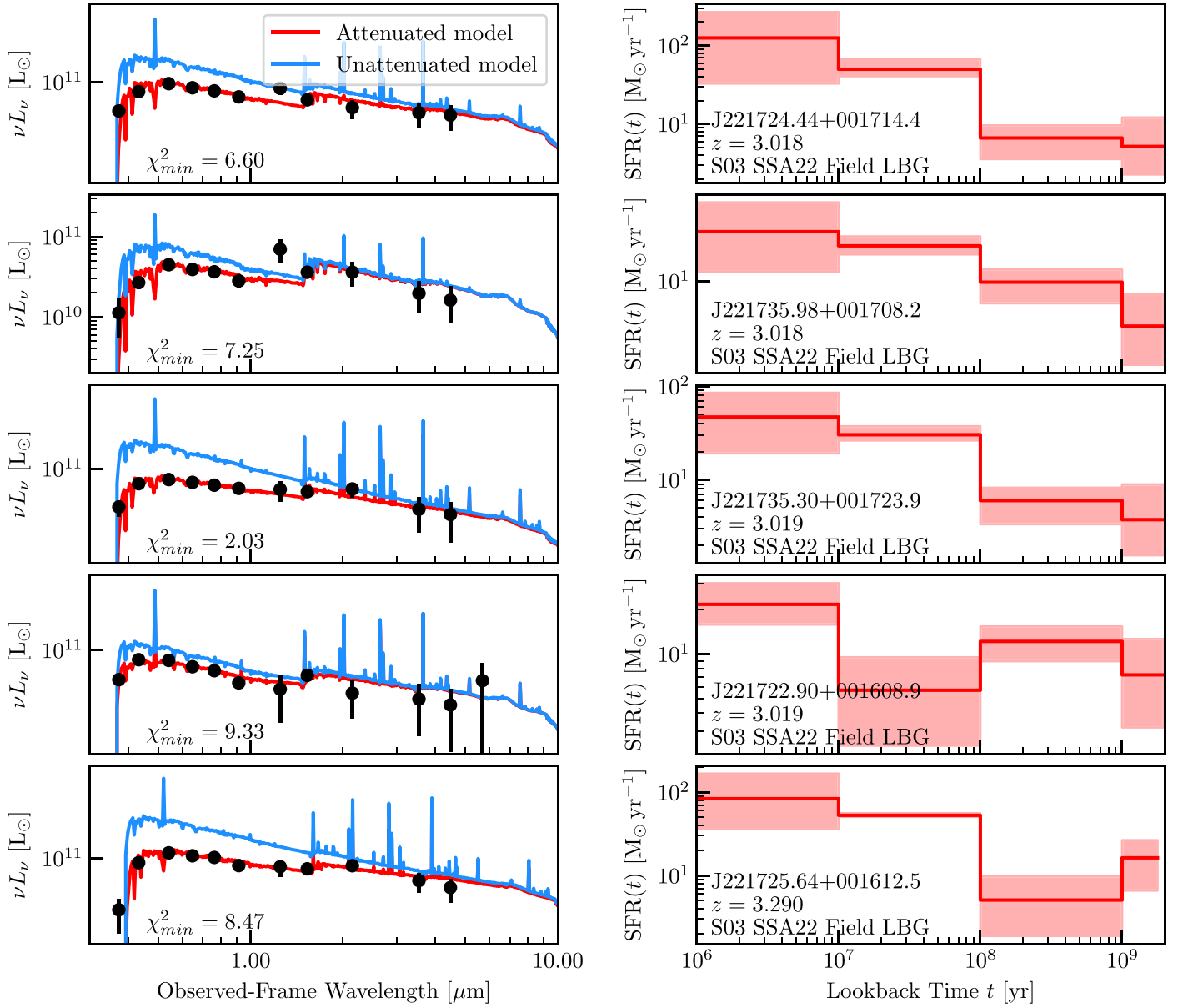


Figure 16. Same as Figure 14, but showing the five S03 SSA22 field LBGs with SED fits.

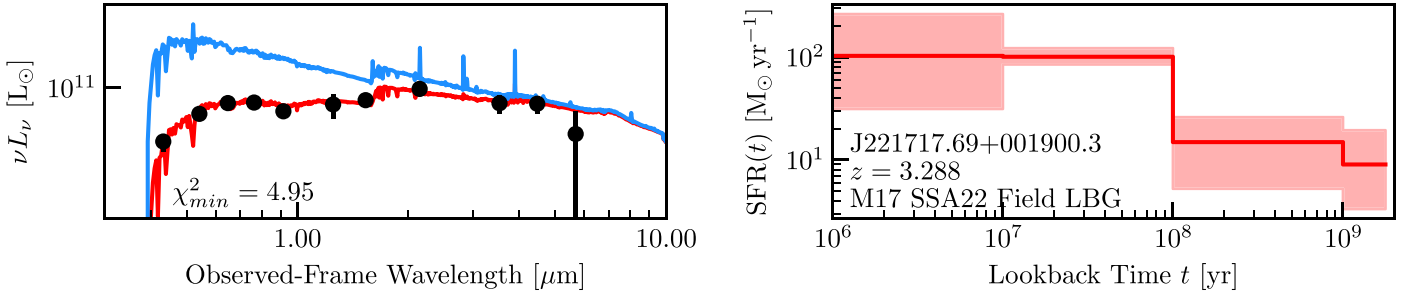


Figure 17. Same as Figure 14, but showing the single M17 SSA22 field LBG with an SED fit.

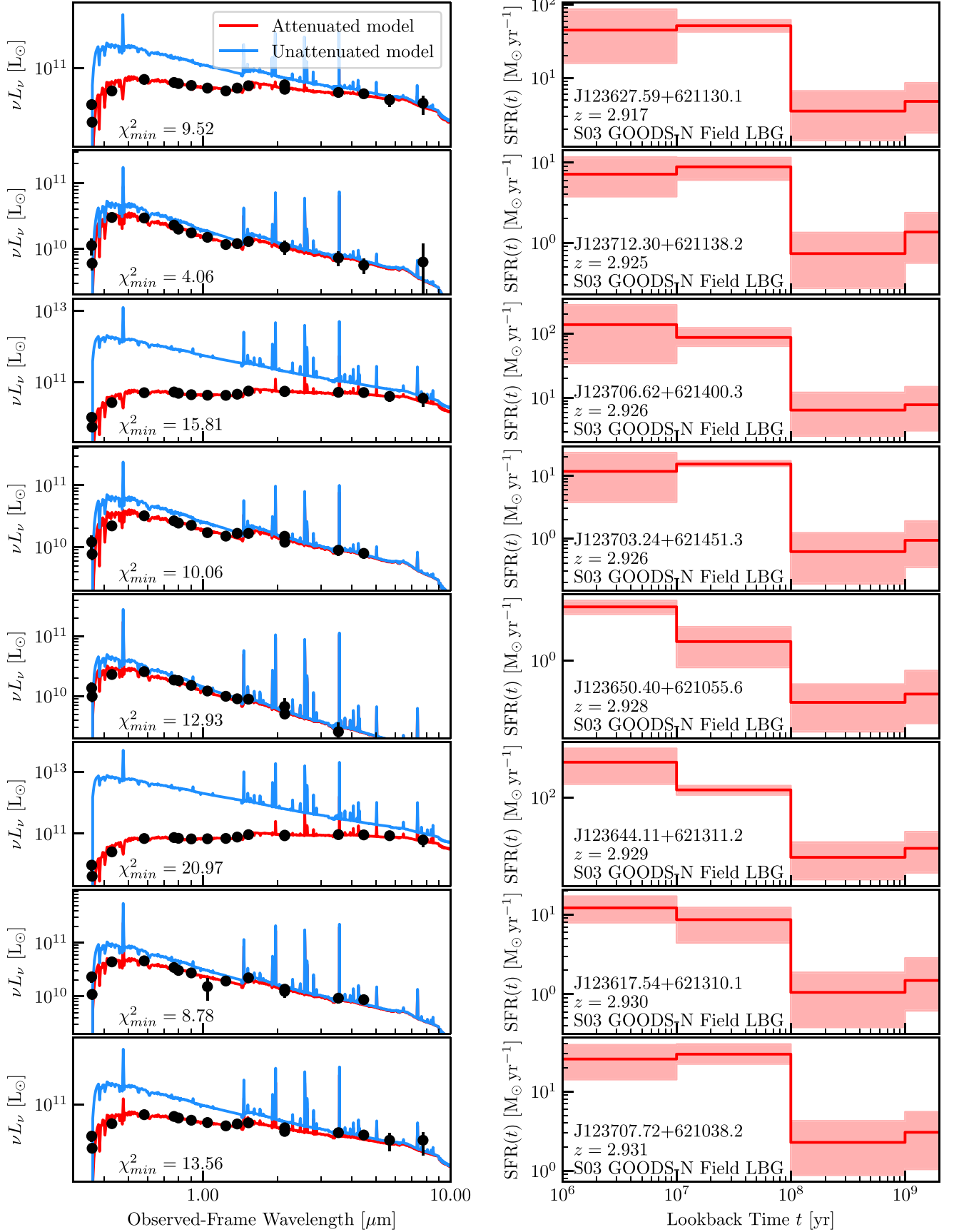



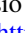

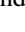





Figure 18. Same as Figure 14, but showing the first eight S03 GOODS-N field LBGs listed in Table 9. We show the SED and SFH fits for the remaining GOODS-N LBGs in the online version of this article. (An extended version of this figure is available.)

ORCID iDs

Erik B. Monson  <https://orcid.org/0000-0001-8473-5140>
 Bret D. Lehmer  <https://orcid.org/0000-0003-2192-3296>
 Keith Doore  <https://orcid.org/0000-0001-5035-4016>
 Rafael T. Eufrasio  <https://orcid.org/0000-0002-2987-1796>
 Brett Bonine  <https://orcid.org/0000-0003-0189-1805>
 David M. Alexander  <https://orcid.org/0000-0002-5896-6313>
 Mariko Kubo  <https://orcid.org/0000-0002-7598-5292>
 Amber Straughn  <https://orcid.org/0000-0002-4772-7878>
 Hideki Umehata  <https://orcid.org/0000-0003-1937-0573>

References

- Abraham, R. G., van den Bergh, S., & Nair, P. 2003, *ApJ*, **588**, 218
 Abruzzo, M. W., Narayanan, D., Davé, R., & Thompson, R. 2018, arXiv:1803.02374
 Alexander, D. M., Simpson, J. M., Harrison, C. M., et al. 2016, *MNRAS*, **461**, 2944
 Astropy Collaboration, Price-Whelan, A. M., Sipőcz, B. M., et al. 2018, *AJ*, **156**, A123
 Astropy Collaboration, Robitaille, T. P., Tollerud, E. J., et al. 2013, *A&A*, **558**, A33
 Barden, M., Häussler, B., Peng, C. Y., McIntosh, D. H., & Guo, Y. 2012, *MNRAS*, **422**, 449
 Barro, G., Pérez-González, P. G., Cava, A., et al. 2019, *ApJS*, **243**, 22
 Bertin, E., & Arnouts, S. 1996, *A&AS*, **117**, 393
 Boylan-Kolchin, M., Springel, V., White, S. D. M., Jenkins, A., & Lemson, G. 2009, *MNRAS*, **398**, 1150
 Calzetti, D., Armus, L., Bohlin, R. C., et al. 2000, *ApJ*, **533**, 682
 Capak, P. L., Riechers, D., Scoville, N. Z., et al. 2011, *Natur*, **470**, 233
 Ceverino, D., Klypin, A., Klimek, E. S., et al. 2014, *MNRAS*, **442**, 1545
 Conselice, C. J., Bershad, M. A., Dickinson, M., & Papovich, C. 2003, *AJ*, **126**, 1183
 Cooke, E. A., Hatch, N. A., Muldrew, S. I., Rigby, E. E., & Kurk, J. D. 2014, *MNRAS*, **440**, 3262
 Cowie, L., Gardner, J., Hu, E., et al. 1994, *ApJ*, **434**, 114
 Daddi, E., Valentino, F., Rich, R. M., et al. 2021, *A&A*, **649**, A78
 Digby-North, J. A., Nandra, K., Laird, E. S., et al. 2010, *MNRAS*, **407**, 846
 Ding, X., Silverman, J., Treu, T., et al. 2020, *ApJ*, **888**, 37
 Doore, K., Eufrasio, R. T., Lehner, B. D., et al. 2021, *ApJ*, submitted
 Eufrasio, R. T., Lehmer, B. D., Zezas, A., et al. 2017, *ApJ*, **851**, 10
 Fakhouri, O., & Ma, C.-P. 2009, *MNRAS*, **394**, 1825
 Ferrarese, L., & Merritt, D. 2000, *ApJL*, **539**, L9
 Fioc, M., & Rocca-Volmerange, B. 1997, *A&A*, **326**, 950
 Fioc, M., & Rocca-Volmerange, B. 1999, arXiv:astro-ph/9912179
 Fitzpatrick, E. L. 1999, *PASP*, **111**, 63
 Fruchter, A. S., et al. 2010, in Space Science Institute Telescope Calibration Workshop, **382**
 Governato, F., Baugh, C. M., Frenk, C. S., et al. 1998, *Natur*, **392**, 359
 Graham, A. W., & Driver, S. P. 2005, *PASA*, **22**, 118
 Grogin, N. A., Kocevski, D. D., Faber, S. M., et al. 2011, *ApJS*, **197**, 35
 Harikane, Y., Ouchi, M., Ono, Y., et al. 2019, *ApJ*, **883**, 142
 Hatch, N. A., Kurk, J. D., Pentericci, L., et al. 2011, *MNRAS*, **415**, 2993
 Häussler, B., Bamford, S. P., Vika, M., et al. 2013, *MNRAS*, **430**, 330
 Häussler, B., McIntosh, D., Barden, M., et al. 2007, *ApJS*, **172**, 615
 Hayashino, T., Matsuda, Y., Tamura, H., et al. 2004, *AJ*, **128**, 2073
 Higuchi, R., Ouchi, M., Ono, Y., et al. 2019, *ApJ*, **879**, 28
 Hine, N. K., Geach, J. E., Alexander, D. M., et al. 2015, *MNRAS*, **455**, 2363
 Iwata, I., Inoue, A. K., Matsuda, Y., et al. 2009, *ApJ*, **692**, 1287
 Kartaltepe, J. S., Dickinson, M., Alexander, D. M., et al. 2012, *ApJ*, **757**, 23
 Kato, Y., Matsuda, Y., Smail, I., et al. 2016, *MNRAS*, **460**, 3861
 Koekemoer, A. M., Faber, S. M., Ferguson, H. C., et al. 2011, *ApJS*, **197**, 36
 Kroupa, P. 2001, *MNRAS*, **322**, 231
 Kubo, M., Uchimoto, Y. K., Yamada, T., et al. 2013, *ApJ*, **778**, 170
 Kubo, M., Yamada, T., Ichikawa, T., et al. 2015a, *ApJ*, **799**, 38
 Kubo, M., Yamada, T., Ichikawa, T., et al. 2015b, *MNRAS*, **455**, 3333
 Kubo, M., Yamada, T., Ichikawa, T., et al. 2017, *MNRAS*, **469**, 2235
 Le Fèvre, O., Cassata, P., Cucciati, O., et al. 2013, *A&A*, **559**, A14
 Lehmer, B. D., Alexander, D. M., Chapman, S. C., et al. 2009a, *MNRAS*, **400**, 299
 Lehmer, B. D., Alexander, D. M., Geach, J. E., et al. 2009b, *ApJ*, **691**, 687
 Lehmer, B. D., Lucy, A. B., Alexander, D. M., et al. 2013, *ApJ*, **765**, 87
 Lotz, J. M., Davis, M., Faber, S. M., et al. 2008, *ApJ*, **672**, 177
 Lotz, J. M., Jonsson, P., Cox, T. J., & Primack, J. R. 2010, *MNRAS*, **404**, 575
 Lotz, J. M., Madau, P., Giallisco, M., Primack, J., & Ferguson, H. C. 2006, *ApJ*, **636**, 592
 Lotz, J. M., Papovich, C., Faber, S. M., et al. 2013, *ApJ*, **773**, 154
 Lotz, J. M., Primack, J., & Madau, P. 2004, *AJ*, **128**, 163
 Madau, P., & Fragos, T. 2017, *ApJ*, **840**, 39
 Mantha, K. B., McIntosh, D. H., Ciaschi, C. P., et al. 2019, *MNRAS*, **486**, 2643
 Martini, P., Miller, E. D., Brodwin, M., et al. 2013, *ApJ*, **768**, 1
 Matsuda, Y., Yamada, T., Hayashino, T., et al. 2004, *AJ*, **128**, 569
 Matsuda, Y., Yamada, T., Hayashino, T., et al. 2005, *ApJL*, **634**, L125
 McAlpine, S., Harrison, C. M., Rosario, D. J., et al. 2020, *MNRAS*, **494**, 5713
 Micheva, G., Iwata, I., Inoue, A. K., et al. 2017, *MNRAS*, **465**, 316
 Miley, G. K., Overzier, R. A., Tsvetanov, Z. I., et al. 2004, *Natur*, **427**, 47
 Narayanan, D., Turk, M., Feldmann, R., et al. 2015, *Natur*, **525**, 496
 Noll, S., Burgarella, D., Giovannoli, E., et al. 2009, *A&A*, **507**, 1793
 Overzier, R. A. 2016, *A&ARv*, **24**, 14
 Peng, C. Y., Ho, L. C., Impey, C. W., & Rix, H.-W. 2002, *AJ*, **124**, 266
 Romano-Díaz, E., Shlosman, I., Choi, J.-H., & Sadoun, R. 2014, *ApJL*, **790**, L32
 Saez, C., Lehmer, B. D., Bauer, F. E., et al. 2015, *MNRAS*, **450**, 2615
 Schlafly, E. F., & Finkbeiner, D. P. 2011, *ApJ*, **737**, 103
 Snyder, G. F., Lotz, J., Moody, C., et al. 2015, *MNRAS*, **451**, 4290
 Steidel, C. C., Adelberger, K. L., Dickinson, M., et al. 1998, *ApJ*, **492**, 428
 Steidel, C. C., Adelberger, K. L., Shapley, A. E., et al. 2000, *ApJ*, **532**, 170
 Steidel, C. C., Adelberger, K. L., Shapley, A. E., et al. 2003, *ApJ*, **592**, 728
 Steidel, C. C., Adelberger, K. L., Shapley, A. E., et al. 2005, *ApJ*, **626**, 44
 Tamura, Y., Iono, D., Wilner, D. J., et al. 2010, *ApJ*, **724**, 1270
 Tamura, Y., Kohno, K., Nakanishi, K., et al. 2009, *Natur*, **459**, 61
 Targett, T. A., Dunlop, J. S., McLure, R. J., et al. 2011, *MNRAS*, **412**, 295
 Toshikawa, J., Kashikawa, N., Overzier, R., et al. 2016, *ApJ*, **826**, 114
 Toshikawa, J., Uchiyama, H., Kashikawa, N., et al. 2018, *PASJ*, **70**, S12
 Trenti, M., Bradley, L., Stiavelli, M., et al. 2012, *ApJ*, **746**, 55
 Umehata, H., Fumagalli, M., Smail, I., et al. 2019, *Sci*, **366**, 97
 Umehata, H., Hatsukade, B., Smail, I., et al. 2018, *PASJ*, **70**, 65
 Umehata, H., Tamura, Y., Kohno, K., et al. 2014, *MNRAS*, **440**, 3462
 Umehata, H., Tamura, Y., Kohno, K., et al. 2015, *ApJL*, **815**, L8
 Umehata, H., Tamura, Y., Kohno, K., et al. 2017, *ApJ*, **835**, 98
 van der Wel, A., Bell, E. F., Häussler, B., et al. 2012, *ApJS*, **203**, 24
 Venemans, B., Kurk, J., Miley, G., et al. 2002, *ApJL*, **569**, L11
 Vika, M., Bamford, S. P., Häussler, B., et al. 2013, *MNRAS*, **435**, 623
 Vito, F., Brandt, W. N., Lehmer, B. D., et al. 2020, *A&A*, **642**, A149
 Wang, T., Schreiber, C., Elbaz, D., et al. 2019, *Natur*, **572**, 211
 Yamada, T., Nakamura, Y., Matsuda, Y., et al. 2012, *AJ*, **143**, 79
 Yang, G., Brandt, W. N., Darvish, B., et al. 2018, *MNRAS*, **480**, 1022
 Zamojski, M., Yan, L., Dasyra, K., et al. 2011, *ApJ*, **730**, 125
 Zibetti, S., Charlot, S., & Rix, H.-W. 2009, *MNRAS*, **400**, 1181
 Zolotov, A., Dekel, A., Mandelker, N., et al. 2015, *MNRAS*, **450**, 2327